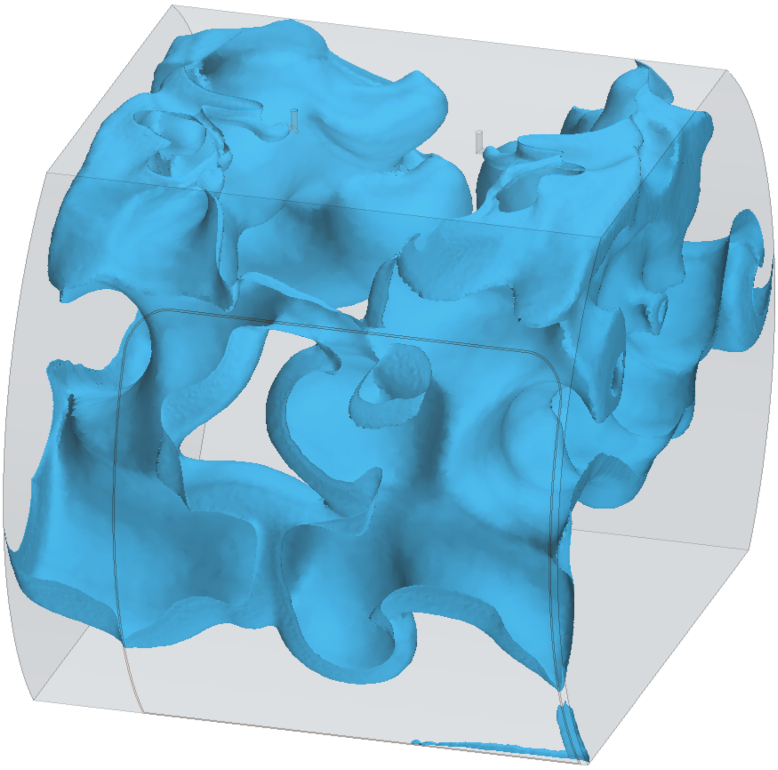

CFD modeling of cargo compartment fire extinguishing system onboard electric aircraft

Master's thesis in Applied Mechanics and Mobility Engineering

JACOB BRILLANTE
LENA IVARSSON

DEPARTMENT OF MECHANICS AND MARITIME SCIENCES
CHALMERS UNIVERSITY OF TECHNOLOGY
Gothenburg, Sweden 2023
www.chalmers.se

Master's thesis 2023

CFD modeling of cargo compartment fire extinguishing system onboard electric aircraft

JACOB BRILLANTE
LENA IVARSSON

Department of Mechanics and Maritime Sciences
Division of Vehicle Engineering and Autonomous Systems
Chalmers University of Technology
Gothenburg, Sweden 2023

CFD modeling of cargo compartment fire extinguishing system onboard electric aircraft
JACOB BRILLANTE
LENA IVARSSON

Supervisor: Anna Sordi, Section Lead Fire Detection and Suppression Systems, Heart Aerospace AB
Supervisor: Sandro Henrique de Morais, Senior Fire Detection and Suppression Systems Engineer, Heart Aerospace AB
Examiner: Simone Sebben, Professor in Aerodynamics at Mechanics and Maritime Sciences, Head of Division of Vehicle Engineering and Autonomous Systems

Master's Thesis 2023
Department of Mechanics and Maritime Sciences (M2)
Division of Vehicle Engineering and Autonomous Systems
Chalmers University of Technology
SE-412 96 Gothenburg
Telephone +46 31 772 1000

Cover: Flow visualisation post-processed in Star-CCM+ demonstrating the distribution of fire extinguishing agent using an isosurface representing mass fraction.

Typeset in LaTeX
Printed by Chalmers Reproservice
Gothenburg, Sweden 2023

CFD modeling of cargo compartment fire extinguishing system onboard electric aircraft
JACOB BRILLANTE
LENA IVARSSON
Department of Mechanics and Maritime Sciences (M2)
Chalmers University of Technology

Abstract

Today, when an aircraft is to be certified and approved to ensure safe flight, a series of physical tests of safety critical systems and components are carried out. Among these systems is the fire suppression system for the cargo compartment of the aircraft. The existing fire extinguishing system designs depend primarily on experience and physical tests. These tests are both costly and time consuming and usually end up with the systems being over dimensioned to ensure they meet the requirements for certification. The aviation industry has seen the potential in applying computational fluid dynamics (CFD) simulation as a scientific design tool for these systems, in order to reduce the number, and thus the cost, of physically performed tests.

The objective of this thesis is to develop a first CFD model of the cargo compartment fire extinguishing system. The model can then be adjusted in terms of parameters and design to optimize the system efficiency before certification testing.

The modeling of the fire extinguishing system is divided into two separate models; one for the discharge bottle and piping system, and one for the cargo compartment. The Halon outlet parameters from the piping system are then used as inlet parameters to the cargo compartment.

The cargo compartment is simulated for four configurations where the inlet flow is varied between being straight or angled and with or without simplified discharge nozzles. The simulations show that an angled discharge of Halon is preferred because it spreads Halon more evenly compared to a straight discharge flow. Among the angled inlet flow and nozzles, 90 degree nozzles provide the highest degree of coverage by having the most probes that detect Halon. It is also this nozzle design that best mimics those designs provided by nozzle suppliers.

Keywords: CFD, firex, firex agent, Halon, single-phase, multiphase, electric airplane, aircraft development.

Acknowledgements

Firstly, we would like to thank Heart Aerospace for giving us this opportunity to conduct this master's thesis at the company. In addition to this, we would also like to thank the Mechanical Systems department at Heart Aerospace, for welcoming us. We would also like to express our gratitude to our supervisors Anna Sordi (Section Lead - Fire Detection and Fire Suppression Systems) and Sandro Henrique de Morais (Senior Fire Detection and Suppression System Engineer) at Heart Aerospace, for all the help and guidance throughout this thesis.

From Chalmers we would like to thank Alexey Vdovin (Researcher at Vehicle Engineering and Autonomous Systems) for consulting on simulation setup and assisting with computing power. Finally, we would like to thank our examiner, Simone Sebben (Professor and head of Vehicle Engineering and Autonomous Systems), for the support and feedback we have received during our thesis.

Lena Ivarsson & Jacob Brillante
Gothenburg, June 2023

List of Acronyms

Below is the list of acronyms that have been used throughout this thesis listed in alphabetical order:

AC	Advisory Circular
AMC	Acceptable Means of Compliance
APU	Auxiliary Power Unit
BCF	Bromochlorodifluoromethane
CAD	Computer Aided Design
CFD	Computational Fluid Dynamics
CFL	Courant-Friedrichs-Lewy
CS	Certification Specification
DNS	Direct Numerical Simulation
EASA	European Union Aviation Safety Agency
ECTS	European Credit Transfer and Accumulation System
EE	Eulerian-Eulerian
EMP	Eulerian Multiphase
EU	European Union
FAA	Federal Aviation Administration
FEM	Finite Element Method
Firex	Fire Extinguishing System
Firex Agent	Fire Extinguishing System Agent
FVM	Finite Volume Method
Halon 1211	Bromochlorodifluoromethane
Halon 1301	Bromotrifluoromethane
ICAO	International Civil Aviation Organization
Li-ion	Lithium-ion
LMP	Lagrangian Multiphase
MMP	Mixture Multiphase
N-S	Navier-Stokes
PAX	Passengers
RANS	Reynolds-Averaged Navier Stokes
SAF	Sustainable Aviation Fuel
SIMPLE	Semi-Implicit Method for Pressure Linked Equations
SST	Shear-Stress Transport

URANS	Unsteady Reynolds-Averaged Navier Stokes
VOF	Volume of Fluid
3D	Three-Dimensional

Nomenclature

Below is the nomenclature of parameters that have been used throughout this thesis.

Parameters

g	Gravitational acceleration $[\mathrm{m} \cdot \mathrm{s}^{-2}]$
μ	Dynamic viscosity $[\mathrm{kg} \cdot \mathrm{m} \cdot \mathrm{s}^{-1}]$
ν	Kinematic viscosity $[\mathrm{m}^2 \cdot \mathrm{s}^{-1}]$
ν_t	Eddy viscosity [-]
ρ	Density $[\mathrm{kg} \cdot \mathrm{m}^{-3}]$
ρ_m	Mixture density $[\mathrm{kg} \cdot \mathrm{m}^{-3}]$
τ_w	Wall shear stress $[\mathrm{N} \cdot \mathrm{m}^{-2}]$
α	Volume fraction [-]
p	Static pressure [Pa]
p_{init}	Initial pressure [Pa]
p_∞	Freestream flow pressure [Pa]
Re	Reynolds number [-]
V	Volume $[\mathrm{m}^3]$
u_∞	Freestream flow velocity $[\mathrm{m} \cdot \mathrm{s}^{-1}]$
$\mathbf{u}$	Velocity $[\mathrm{m} \cdot \mathrm{s}^{-1}]$
$\mathbf{S}$	Momentum Source term $[\mathrm{N} \cdot \mathrm{m}^{-3}]$
y^+	Dimensionless wall distance [-]
v	Velocity $[\mathrm{m} \cdot \mathrm{s}^{-1}]$
t	Time [s]
x	x-location [-]
y	y-location [-]
k	Turbulence Kinetic Energy [-]
ε	Turbulence Dissipation Rate [-]

ω	Specific Turbulence Dissipation Rate [-]

Contents

List of Figures

List of Tables

1

Introduction

This chapter presents an introduction to the study performed in the thesis. It presents the background, problem, objective and limitations of the study. The aircraft studied in this thesis is also introduced and explained briefly. In addition to this, the outline of the thesis is also included in this chapter.

1.1 Background

Rapid expansion of air travel, especially within civil aviation, in the last four decades has led to an increase in global greenhouse gas emissions. In 2018, emissions from aviation accounted for 918 million tonnes of CO_2. This corresponds to approximately 2.4% of the human-caused global CO_2 emissions [1]. Compared to other means of transportation, such as the automotive sector, the aviation industry accounts for a considerably smaller emission contribution. In 2021, passenger cars accounted for 39% and trucks 23% of the CO_2 emissions by the transport sector, while aviation accounted for 9% [2]. However, the automotive industry is currently undergoing a major energy transformation with hybrid and electric vehicles that will result in greatly reduced CO_2 emissions. Given this, aviation will account for a greater proportion of the emissions if nothing drastic happens soon in the aviation industry. During the COVID-19 outbreak in 2020, a radical drop in the number of flights (and thereby in global greenhouse gas emissions) could be seen. However, forecasts show that the amount of air travel will most likely increase significantly within the next few decades [3]. This requires action from the aviation industry and those who manufacture aircraft, in order to continue to enable this mode of transportation in the future.

To counteract this trend, the aviation industry is in need of new technology and new generations of aircraft. Currently, the industry is investigating and moving towards, among other things, using biofuels, hydrogen gas and electric aircraft. In 2017, the Swedish government created a framework of climate reformations in line with the Paris Agreement. In this framework, it is stated that all domestic air transport shall be fossil-free by 2030 [4]. By 2040, all short-haul flights in Norway aim to be electric [5]. Electrification of aircraft is therefore one of several technological solutions towards net zero carbon emissions. This thesis is carried out together with Heart Aerospace, a Swedish tech start up company aiming to develop and manufacture electric aircraft.

Fire safety on board an aircraft is among the most important considerations in aircraft design. For an aircraft to even be allowed to take off, a fire detection and fire extinguishing (firex) system, must be installed in the areas of the aircraft most at risk of catching fire. To effectively extinguish the fire that may occur, the placement and number of discharge nozzles, together with the quantity of the fire extinguishing agent (firex agent) released must be analyzed and tested to ensure that the firex system works as intended. Before an aircraft goes into service, the aircraft must be in condition for safe operation, i.e. be considered as airworthy [6]. For an aircraft to comply with the airworthiness authorities' certification requirements, the aircraft manufacturer must prove that the firex system of the aircraft, in the event of a fire, can maintain a certain amount of firex agent concentration. Traditionally, these systems are designed to pass the physical tests conducted both at ground level and in flight. In the design of firex systems, the potential of applying Computational Fluid Dynamics (CFD), has been seen. Airbus developed a CFD model of the cargo compartment of an A350-900, together with its firex system. Both the European Union Aviation Safety Agency (EASA) and the Federal Aviation Administration (FAA) have accepted CFD as an adequate tool, a so called acceptable means of compliance (AMC) [7]. By simulating the firex system, the development time can be greatly reduced, leading to that the dimensioning of the system can be optimized while the cost and time for physical testing can be significantly reduced.

1.2 About the ES-30 Aircraft

The aircraft considered in this thesis is a short-haul commercial hybrid-electric airplane, the ES-30. A concept rendering of the aircraft, provided by Heart Aerospace [8], can be seen in Figure 1.1. The aircraft will be certified to EASA Certification Specification 25 (CS-25), which is EASA's certification specification for large airplanes, and will seat 30 passengers (PAX) in a 2+1 seating configuration. The cargo compartment of the aircraft is designed according to the industry standard of 25 kg of luggage per passenger. The rechargeable batteries will be placed underneath the aircraft, in its so called belly. These batteries will feed energy to the four electric motors placed at each propeller on the wings. The aircraft must fulfill the need of a reserve, for instance in case of weather or traffic variability forcing the aircraft to be redirected to a different airport than intended. On the ES-30, this reserve will consist of two turbo generators in the aft fuselage, being fed with sustainable aviation fuel (SAF) located on the wings, which in turn feed the electric system with energy. The reserve system will, if necessary, extend the range of the aircraft from 200 km full-electric range to 400 km hybrid-electric range. As the energy content of lithium-ion (Li-ion) batteries will increase, together with its price reduction, the intention of the company is to provide aircraft with longer range. However, the current range is considered sufficient to cover the vast majority of short-haul routes. The ES-30 will enter commercial service in 2028 [8].

Figure 1.1: *Concept rendering of the ES-30 aircraft.*

1.3 Objective

The objective of the thesis is to produce a CFD model, representing a cargo compartment and its fire extinguishing system. The cargo and fire extinguishing system, even though based on a given aircraft design (the ES-30) at Heart Aerospace, is a generic configuration. This model should then be used to simulate the fire extinguishing system in terms of agent distribution.

1.4 Working Methods

The thesis begins with a literature study of current firex agents and firex systems. This review will then be followed by preparing the Computer Aided Design (CAD) models to be used in the simulations. In order to validate the simulations, correlation with experimental data is needed. Since the ES-30 is not built at the time of this thesis, no experimental data is available from the stakeholder. Instead, a reliable source of this data must be found in order to validate the model. The main part of the thesis will consist of creating models of the system and setting up and making the simulations as realistic as possible. After the preparation and setup period, the model will be used to study different nozzle configurations. The results will then be analyzed and used as the basis for proposing future simulation methods and design recommendations for the extinguishing system, thus reducing physical testing.

1.5 Limitations

The thesis is limited in some regards. Only the cargo compartment will be modeled and analyzed. The thesis will not include any physical testing, it will only be visualized in three dimensions using CAD and simulated using CFD. Therefore, the numerical results produced cannot be validated. The design representing the cargo compartment of the ES-30, that will be used for simulation, will be generic. Given that the thesis will only consider simulation, the thesis will only consider numerical solutions to the problem.

There are both passive and active approaches to extinguishing fires on an aircraft. In this thesis, the focus will be on active firex systems, such as smoke and fire detectors, fire suppression systems, ventilation control and automatic shutdown of systems. Passive features primarily involve the use of non-combustible and/or self-extinguishing materials and fire-resistant cargo liners, but will not be part of the thesis. In this thesis, only built-in firex installations will be considered. Handheld extinguishers will therefore not be considered in this thesis.

A fire will not be simulated in this thesis. This is mainly due to that it is not necessary for testing the firex system. When physically testing and verifying the extinguishing system, a fire will not be present. Instead, only concentration measures of the extinguishing agent will be conducted. As described more in detail in Section 2.1.2.1, the firex system consist of two discharge bottles containing firex agent. In this thesis, only one discharge will be simulated reproducing the initial, so called, “high-rate” discharge. The second, so called, “low rate” discharge will not be simulated due to the computational power that would be required. To be able to capture the behaviour of the second discharge, a total physical time corresponding to 30 seconds would need to be simulated, which would be too computationally heavy and time consuming for this thesis.

1.6 Thesis Outline

The thesis is divided into six chapters. To give the reader an overview of the report, the different parts of the report are described below:

Chapter 1 - Introduction provides an introduction to the scope of the thesis. It also includes a background describing the relevance of electric aviation and applying CFD simulations in the field of fire protection systems in the aviation industry.

Chapter 2 - Theory present the current firex systems as well as necessary theories behind fluid dynamics and CFD modelling approaches.

Chapter 3 - Methodology describes the methods used in this thesis more in detail. This includes the process and model preparation steps in both CAD and CFD.

Chapter 4 - Results & Analysis presents the results generated in the thesis work. Most importantly, the majority of the results will include the simulation results obtained from CFD. In connection with the presentation of the results, analyzes of the results will also take place in this chapter.

Chapter 5 - Discussion discusses the overall challenges experienced in the thesis.

Chapter 6 - Conclusion gives a summary and will draw the conclusions of the thesis, together with suggestions for further work.

2

Theory

In the following chapter, the theory needed to understand the methods and the results obtained in the thesis is described. The chapter begins by describing the current aircraft fire extinguishing system, with associated extinguishing agent, for the cargo compartment. Further, the fundamental fluid dynamics phenomena and CFD theory relevant for the thesis are described.

2.1 Aircraft Fire Extinguishing System

Fire onboard an aircraft is among the most safety critical situations that can occur, both on ground and during flight. It is crucial how early the fire can be detected and consequently extinguished to minimize its damage. The type of firex system depends on where the fire originates. Among the areas most prone to catching fire in an aircraft is the cargo compartment area, the auxiliary power unit (APU), the engine, the cockpit, the cabin and the lavatory.

2.1.1 Extinguishing Agents

Depending on the type of fire, the extinguishing agent used on an aircraft might differ. According to EASA CS-25, there are three fire classifications defined, depending on the substance that burns [9]:

- **Class A:** Fires caused by commonly used combustibles, such as wood, paper, rubber, plastic etc.
- **Class B:** Fires caused by flammable liquids, such as petroleum oils, alcohols, flammable gases etc.
- **Class C:** Fires involving electrical equipment.

Bromotrifluoromethane ($CBrF_3$), also known as Halon 1301 and hereafter referred to as “Halon”, is the only option available for engine, APU and cargo applications. Halon is stored as liquefied gas in steel bottles pressurised with nitrogen. The pressurisation assists with rapid expulsion. Halon is a form of hydrocarbon that, in addition to hydrogen and carbon, consists of chlorine, fluorine, bromine and/or iodine. As a fire extinguishing agent, it prevents spreading of fire by chemically disrupting combustion. This results in very efficient extinguishing effect. Furthermore, Halon 1301 evaporates cleanly and does not cause damage to structure (e.g.

corrosion or surface coating damages) after being in contact. The absence of residue is suitable for safe use on electrical circuits as well as simplifies the cleaning of the compartment afterwards. The drawback of Halon is its high ozone layer depletion, resulting in damage to the ozone layer when released into the atmosphere.

As a result of discovering its negative environmental impact, non-essential use of Halon has been eliminated. In Europe, Halon extinguishers are only allowed in some application areas, such as aircraft, helicopter and submarine applications in case of approved exemption from authorities. For portable extinguishers, bromochlorodifluoromethane (BCF) also known as Halon 1211, was used until 2014. Since then, Halon 1211 has been replaced by other products marketed as Halotron BrX™ (2-BTP) and HFC-227ea (FM-200). The search for alternative agents for Halon 1301 is ongoing, but it has been proved difficult finding alternatives of comparable effectiveness [10]. Trifluoroiodomethane (CF_3I) shares chemical similarities to Halon and has been considered a potential replacement due to being more environmentally friendly [11]. However, it has only been considered a replacement for engine and APU firex systems, due to being a potential toxicant. Working groups formed by certification authorities and the aviation industry are proposing standards for new agents such as CF_3I, but there are still installation challenges related to toxicity and performance in varying aircraft conditions.

2.1.2 Cargo Compartment

The cargo compartment is a pressurized space storing luggage and/or goods on the aircraft.

Particularly for the cargo compartment, the phrase “suppression system” is more usual than “extinguishing system”. This is due to that the system is not required to completely extinguish a fire in this area of the aircraft. Instead, the purpose of the system is to suppress a fire until the aircraft has landed safely and ground personnel can identify the source of the fire and fully extinguish it [12]. However, the terms “extinguishing system” and “suppression system” are used interchangeably as per an Advisory Circular (AC) issued by the FAA [13].

Just as there are classifications of fire, there are classifications of cargo compartments. Depending on the classification of cargo compartment, different fire suppression systems are required. According to EASA CS-25, there are five categories of cargo compartments [9]:

- **Class A:** Cargo compartment located close to flight crew, enabling the fire to be easily detected and extinguished with handheld extinguisher.
- **Class B:** Cargo compartment having smoke or fire detection system to warn pilot. Still accessible enough compartment for a crew member to extinguish.
- **Class C:** No requirement for compartment to be accessible for a crew member. Cargo compartment must therefore be equipped with both smoke or fire detection system and built-in fire suppression system controlled from cockpit.
- **Class E (only allowed on aircraft strictly used for carrying cargo):**

Cargo compartment equipped with smoke or fire detection system to warn pilot. Not required to have a built-in fire suppression system. The fire is controlled by shutting off the ventilating airflow and gradually depressurize the airplane to limit the oxygen supply until the airplane can descend to land.

- **Class F:** Cargo compartment located on main deck equipped with smoke or fire detection system to warn pilot. Must provide means to control the fire which does not require a crewmember to enter compartment. There must be means to seal smoke, flames and firex agent from any compartment which may be occupied by crew or passengers.

Up until 1998, a Class D cargo compartment existed before it was distributed between Class C or Class E [14].

The cargo compartment on the ES-30, would in its current state be classified as a Class C compartment.

2.1.2.1 Fire Suppression Procedure

The cargo fire suppression system is usually a metered system with a flow regulator. This system consists of high- and low-rate bottles that portion firex agent out via pipes into nozzles located in the ceiling of the cargo compartment. The system is designed to keep the fire suppressed for continued safe flight and landing at the nearest suitable airport. A simplified schematic of the system is shown in Figure 2.1.

The sequence of events to suppress a fire within a cargo compartment classified as Class C is generally divided into two steps. The fire suppression system is activated only after the smoke detectors have identified fire and consequently warned cockpit and shut down the airflow to the cargo compartment. The pilot must then actively discharge the fire extinguishing bottles by pushing a button. Initially, the suppression system has a high-rate knockdown discharge to knock down flames and suppress the fire. To ensure that the fire is suppressed, a minimum of 5% Halon concentration by volume must be added via the high-rate discharge. To maintain a suppressed fire, a second low-rate, flow metered, discharge is then triggered. This discharge ensures that the Halon concentration does not reduce below 3% by volume until the aircraft has landed [9]. Testing at the FAA Technical Center together with other fire extinguishing evaluation tests have shown that the core of the fire could remain hot for a period of time and if there is sufficient oxygen available - there is a risk of re-ignition. To avoid re-ignition, the concentration of Halon has, therefore, been proven to not be allowed to drop below 3% by volume [9]. There is no firm requirement for how long it may take before triggering the second discharge, but from communication with fire protection system engineers, a time span of 20-30 seconds after the initial knockdown discharge is suggested as a reasonable assumption. Therefore, the most important is to guarantee that the agent concentration would be kept above 3% during all time.

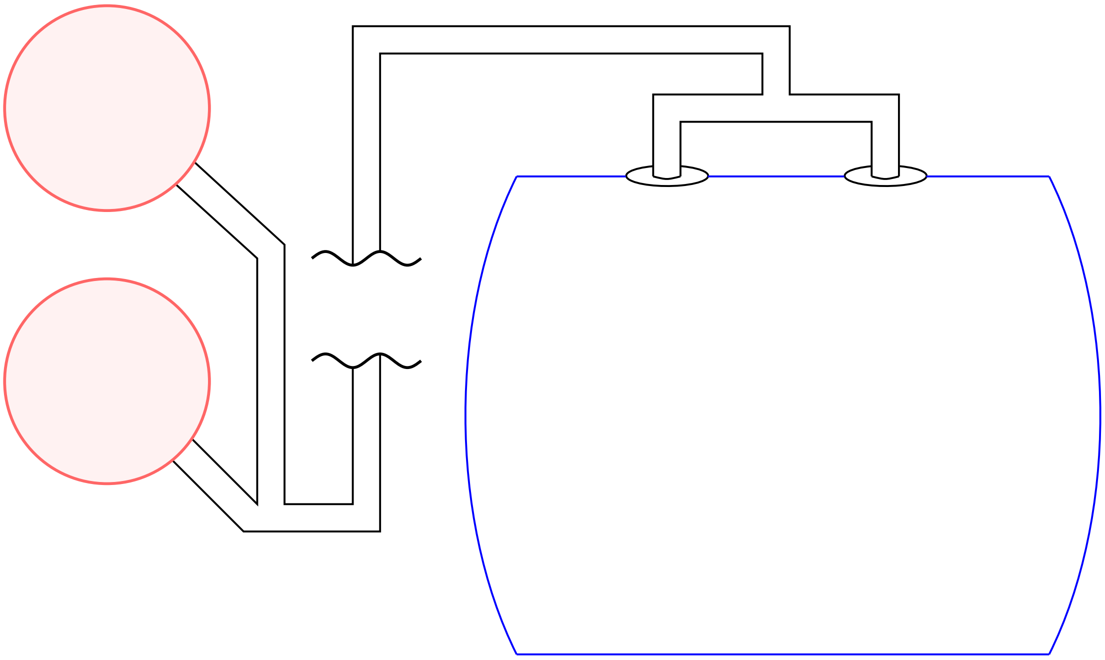

Figure 2.1: *Schematic of cargo compartment fire extinguishing system. Discharge bottle (red), piping (black) and cargo compartment (blue). Note that the components are not shown in the same scale.*

2.1.2.2 Concentration Measurements of Fire Extinguishing Agent

To demonstrate that the cargo compartment firex system works as intended, flight tests are carried out. To monitor the concentration of firex agent in the cargo compartment, continuous measurements in this space are required. Therefore, guidance concerning the installation of concentration measuring probes in conjunction with measuring the concentration of firex agent for a cargo compartment is given in an AC published by FAA [13].

During testing 12 probes are placed accordingly, each connected to an analyzer, also known as Halonyzer, measuring the concentration. The positioning of the sampling probes should be normal to the anticipated local airflow. The probes should not be positioned close to the agent discharge nozzles due to the risk that the probes register higher concentration measures than the actual concentration expected in this area. However, they should be placed as close as practically possible to potential leakage or ventilation flow areas such as door seals and vents, since leakage can affect local concentration levels. Furthermore, the sampling locations must be spread in different vertical, horizontal and longitudinal locations. This results in a grid of probes with sufficient resolution to acquire the variations in concentration levels throughout the cargo compartment.

Additionally, the firex system must provide sufficient concentration of Halon to suppress eventual fires anywhere luggage and cargo might be placed, for the time duration required to land and evacuate the aircraft. The highest probes should also be, at least, placed at a height corresponding to the highest loading point of cargo [9]. Halon will stratify shortly after being discharged into the cargo compartment.

This is mainly because Halon is approximately five times heavier than air, but also due to temperature differences and ventilation. The firex agent also has a tendency to move forward or rearward within the compartment during flight, depending on the pitch of the airplane. Therefore, the firex concentration in the upper part of the compartment will decay faster compared to the lower locations.

During flight testing, climb and descent phases provide very dynamic environments and are challenging for accurate data acquisition. Moreover, compliance demonstration should include data acquired after a sufficiently long time duration representing a landing and complete evacuation phase of the aircraft [9]. Finally, the cargo compartment should be empty during certification testing. By testing the system with an empty cargo compartment, the volume which must be filled by Halon is the largest and therefore the most difficult condition.

2.2 Single-phase and Multiphase Flow

In fluid mechanics, it is typically single phase flow that is first introduced and covered in courses and literature, where phase refers to the state of matter i.e. solid, liquid or gas. With single phase theory it is possible to evaluate many different types of flow, such as flow around an airfoil. It is an important distinction to make, that only one phase may be present in the observed domain. However, models of single phase flows can be divided into either single- or multicomponent models depending on whether there are several substances in the same phase present in the domain. Nevertheless, in many real applications it is not enough to only consider one phase when modeling a flow. For this reason, modeling approaches must be expanded to include what is known as multiphase flow.

Multiphase flow is a flow where two or more phases exist simultaneously within the same domain. Typically, multiphase flows are divided into one of four categories depending on the interacting phases such as gas-liquid, liquid-solid, gas-solid and three-phase flows. These flows can further be categorised by visual approach, where they may be considered as separated, mixed or dispersed flows.

2.2.1 Eulerian and Lagrangian Frames of Reference

Typically for single phase fluid flow analysis, it is the fluid motion through a given control volume that is of interest. For multiphase flows this is not always the case, where sometimes the individual actions of fluid molecules may be of significance. To describe the fluid flows from such different perspectives, the Eulerian and Lagrangian frames of reference are introduced. The Eulerian concept is to treat the fluid as a field, while the Lagrangian concept is to observe individual fluid particles. Of course, the frameworks have different capabilities and limitations.

There is a fundamental mechanism of Eulerian and Lagrangian frameworks, which allows the two to communicate. When evaluating a property of a field at a given point R within the Eulerian framework, the property of a particle at the same point R must be the same when observed within the Lagrangian framework.

It is also possible to compare the different frameworks in terms of scale, where scale in this context implies both the size of the considered domain and level of information obtained. Naturally, any attempt to acquire information on the scale of individual particles will require more work than trying to predict a field. Such a large amount of information might not be necessary to know either, obviously depending on the case study.

2.2.2 Modeling Approaches

Within the Eulerian and Lagrangian frameworks there exists several different methods, each with a different concept or main idea. Due to being developed with various aims and purposes, many models are not necessarily applicable for all types of problems that may be of interest.

2.2.2.1 Multicomponent Gas Model

The multicomponent gas model is one single phase model used to simulate a miscible mixture consisting of two or more pure gases. The corresponding model also exists for liquids and is therefore named “multicomponent liquid model”. Both multicomponent gas- and liquid model are variants of multicomponent mixture models.

2.2.2.2 Mixture Multiphase

The mixture multiphase (MMP) model is a multiphase, Eulerian, model for dispersed continuous phase interactions. The model originates from the Eulerian multiphase (EMP) model, which is the most complete Eulerian model. For the EMP model, the conservation equations for mass, energy and momentum are treated separately for each phase, which increases the number of equations needed to be solved. The EMP model can therefore be too computationally heavy to solve for some applications, leading to that other models, such as the MMP model, are more suitable [15].

2.2.2.3 Volume of Fluid

The volume of fluid (VOF) model is a method belonging to the Eulerian-Eulerian (EE) framework. The EE approach treats both phases as a continuum. The main goal of VOF is to capture and track the interface between two phases. An indicator function, also known as a colour function, is applied to identify which phase is present within a control volume. The colour function carries a value of either 0 or 1 when there is a single phase present. It follows that a value between 0 and 1 signifies the presence of an interface.

The governing equations solved by the VOF method read

$$\frac{\partial \rho_m}{\partial t} + \nabla \cdot (\rho_m \mathbf{u}) = 0 \tag{2.1}$$

$$\frac{\partial \rho_m \mathbf{u}}{\partial t} + \nabla \cdot (\rho_m \mathbf{u}\mathbf{u}) = -\nabla P + \nabla \boldsymbol{\tau} + \rho_m \mathbf{g} + \mathbf{S} = 0 \tag{2.2}$$

$$\frac{\partial \alpha}{\partial t} + \nabla \left(\alpha \mathbf{u} \right) = 0 \tag{2.3}$$

with $\rho_m = \sum \alpha_k \rho_k$. The subscript m refers to mixture properties and an assumption is made that the two phases share the same field values. It is important to recognise that VOF is not a flow-solving model on its own, but rather a scheme that allows tracking of an interface. The Navier-Stokes (N-S) equations still need to be solved separately. Regarding the interface, the sharpness of the interface is dependent on the resolution of the mesh where a finer mesh results in a sharper interface.

2.3 Numerical Methods for Continuum Flow

In order to predict internal and external continuous fluid flows there are several methods available, each with increasing levels of accuracy and complexity. Typically, an increase of accuracy is associated with complexity, also leading to an increased solving time. Consequently, choosing a method and level of fidelity is often about finding an acceptable compromise between accuracy and cost of simulation.

However, it is important to note that while different, most methods are derived from the N-S equations. While many methods are widely applicable for several types of problems, some have been developed for very specific cases.

2.3.1 Governing Equations

For an incompressible fluid, the flow can be predicted by solving the N-S equations. The N-S equations read

$$\frac{\partial v_i}{\partial x_i} = 0 \tag{2.4}$$

$$\frac{\partial v_i}{\partial t} + \frac{\partial v_i v_j}{\partial v_j} = -\frac{1}{\rho} \frac{\partial p}{\partial x_j} + \nu \frac{\partial^2 v_i}{\partial x_i x_j} \tag{2.5}$$

where Equation 2.4 is known as the continuity equation and Equation 2.5 is known as the momentum equation.

In order to solve a flow problem numerically, the aim is to establish a linear equation system that can be solved. First, the N-S equations are discretised using the Finite-Volume Method (FVM). With the discretised N-S equations, a differencing scheme may be applied in order to describe the convective and diffusive contributions for a given control volume to and from its neighbours. The resulting linear equation system can then be solved iteratively.

When solving the equation system, an issue arises where velocity appears in the continuity equation but not pressure. There are two possible solution methods available, either segregated or coupled. For coupled methods, the continuity and momentum equations are solved simultaneously. For segregated methods, the equations are solved separately and sequentially, instead using an algorithm such as Semi-Implicit Method for Pressure Linked Equations (SIMPLE) to couple pressure and velocity. First, the algorithm solves the momentum equations for velocity, allowing the computation of a mass flux error. A pressure correction equation is then solved, updating the pressure field until the mass fluxes and velocity field are corrected enough to satisfy continuity.

With the described method of discretization and coupling of equations, it is possible to solve the N-S equations numerically. However, directly solving the N-S equations in this manner is extremely computationally expensive. This approach is known as "Direct Numerical Simulation" (DNS) and requires a mesh that allows even the smallest spatial and temporal scales to be resolved. To complete such a simulation, the number of floating-point operations grows with Re^3, where Re is the Reynolds number. For engineering cases, the required computational resources far exceed what is available from supercomputers or clusters. Therefore, simplifications of the N-S equations are necessary in order to solve flow problems present in engineering applications at a reasonable cost. However, a certain level of accuracy must still be maintained.

2.3.1.1 Turbulence Modeling

Another complexity that must be considered is turbulence, which appears in almost all engineering applications. Both external and internal flows may exhibit turbulence, such as in boundary layers or wakes. In order to retain accuracy while reducing computational cost, the Reynolds Averaged Navier-Stokes (RANS) equations are applied.

Averaging introduces new unknown variables, so another relation known as the Boussinesq assumption is introduced in order to close the RANS equations. A new term known as the "eddy" viscosity, ν_t, relates stress to fluid motion. Now, eddy viscosity models are introduced to close the term.

There exists a variety of eddy viscosity models, where variations of the $k - \varepsilon$ and $k - \omega$ models are most commonly applied. The quantities k, ε and ω are known as turbulent kinetic energy, turbulent dissipation rate and specific turbulence dissipation rate respectively. The $k - \varepsilon$ model features two formulations, known as "Standard" $k - \varepsilon$ and "Realisable" $k - \varepsilon$. The main difference is the calculation of the eddy viscosity. Standard $k - \varepsilon$ features a constant dynamic viscosity coefficient, which is instead non-constant for Realizable $k - \varepsilon$.

Both variations are less accurate than $k - \omega$ in adverse pressure gradient regions and close to the wall. However, $k - \varepsilon$ shows good prediction of free-shear flows where pressure gradients are relatively small. An improvement of both models was proposed [16], known as the Shear-Stress Transport (SST) $k - \omega$ model. SST $k - \omega$ combines both models, applying $k - \omega$ in the inner region of the boundary layer before switching to $k - \varepsilon$ in both the outer region of the boundary layer and outside of it.

Both $k - \varepsilon$ and $k - \omega$ are found in most commercial CFD codes and are the most common turbulence models used [17], [18].

2.3.1.2 Flow Near Wall

For cases of turbulent flow, there exists three distinct regions near a wall, the wall layer, overlap layer and outer layer. These regions are differentiated by the type of shear stress that are dominant, leading to different velocity profiles for each region depending on the wall distance. In the wall layer, viscous shear is large and turbulent shear small. For the outer layer it is the opposite. The overlap layer exhibits a mix of the shear stresses. The wall distance y^+ is denoted as a dimensionless quantity, given in Equation 2.6

$$y^+ = \frac{yu^*}{\nu} \tag{2.6}$$

with $u^* = \sqrt{\tau_\omega/\rho}$, τ_ω as the wall shear stress, y as position, ν as viscosity and ρ as density. To describe the different velocity profiles, a non-dimensionalised "velocity", u^+, is defined as

$$u^+ = \frac{u}{u^*} = F(y^+) \tag{2.7}$$

where Equation 2.7 is also known as the "law of the wall". F denotes u^+ as a function of y^+ and a velocity u. In the wall layer, where $0 \leq y^+ \leq 5$, the wall law relation reads

$$u^+ = \frac{u}{u^*} = y^+ \tag{2.8}$$

For the overlap layer, where $30 \leq y^+ \leq 10^3$ the wall law relation reads

$$u^+ = \frac{1}{\kappa}\ln y^+ + B \tag{2.9}$$

where dimensionless constants $\kappa \approx 0.41$ and $B \approx 5.0$. Note that for $5 < y^+ < 30$ there is no relation to describe u^+, making the profile difficult to model. Although, experiments show that the velocity profile will curve, in order to match between the wall layer and overlap layer.

Modeling flow near wall is closely related to the chosen turbulence model and wall treatment, which has heavy implications for the mesh. Prismatic layers may be introduced, to increase the resolution of the mesh near and along the wall. This allows capturing the significant velocity gradients and controlling the y^+ values along surfaces, which is important for turbulence modelling. Typically, when using a $k - \omega$ model to model turbulence, the aim is to achieve $y^+ < 1$. This requires a well resolved prism layer mesh, which increases cell count.

2.3.2 Verification and Validation

In common language, the terms verification and validation are often used interchangeably. However, for computational simulations they cover entirely different concepts and means of determining accuracy and robustness [19]. To distinguish the two terms, verification and validation can briefly be described as "solving the equations right" and "solving the right equations" [20].

For validation, it is also important to recognise a difference between validation of outcomes and CFD code, respectively. From validation, specific outcomes from a model are validated, not all of the code or model. Although, validation may give a developer confidence that a model can to some extent anticipate the behaviour of a system, even when operating outside of the conditions for which a model was originally validated. Unfortunately, as the complexity of a model increases, it may become more difficult to confidently arrive to any conclusion without validation.

A common challenge of applying CFD in industrial applications occurs when CFD is used as a driver in design. In early stages of design, there may be very little possibility for validation experiments. In other cases it may be difficult to scale down a large system into doable experiments, without losing vital properties. In such cases it is important to at least verify the model is solved correctly.

3

Methodology

The methods used in the thesis are presented in this chapter. The chapter begins with the search for a study for validation, followed by post-processing of the simulation models using both CAD and CFD.

3.1 Validation Study

Before any application of CFD simulations, it is important to know what opportunities exist for validation. As previously described, CFD may give a prediction of flow but it is impossible to rely purely on simulation without validation. For the case of simulating a firex system for the ES-30 cargo compartment, it was difficult to validate when there was no airplane or physical cargo compartment built for testing at the time of conducting this thesis.

Therefore, it was ideal to find either a similar case for validation or identify a part of the simulation that could be validated with other experiments or studies. There were a few studies investigating the transport of firex agent from the discharge bottle through a piping system. Liu et al. [21] used Star-CCM+ to simulate firex agent transport in piping and investigate concentration of the agent in an engine nacelle. Kim et al. [22] used Ansys FLUENT to conduct a similar numerical analysis of agent transport in piping. Unfortunately, the studies conducting CFD simulations of bottle and piping lack experimental studies for validation. Amatriain et al. [23] demonstrated the possibility of using a mathematical model, accounting for the multiphase nature of the problem and solving the corresponding governing equations. A study by Elliott et al. [24] was the only study found, in which the firex and bottle piping system is modeled and experiments are performed for validation. The same experimental data was actually used by Amatriain et al. for validation of their model.

Having found experimental data for a part of the firex system, it was decided that the bottle and piping would be simulated separately from the cargo compartment. With a model developed following the experimental setup, it was possible to use the given data for validation. After validation, different piping geometry could be implemented, without losing too much confidence in the model's ability of predicting the agent transport. By the same logic, it was envisioned that the same model physics should be applicable for the cargo compartment case. However, it was noted that in the piping, Halon exists as a liquid before changing phase somewhere along the way, entering the cargo compartment as a gas. This meant that the nature of the cargo compartment case and by extension the applicable methods, were entirely different to that of the piping.

Despite the inability to share physics models, simulations of the piping system were still valuable for analysing firex agent distribution in the cargo compartment. Most important was the resulting mass flow at the end of the piping system which can be assumed as the inlet conditions for the cargo compartment simulation. Naturally, this directly influences how much Halon was present in the cargo compartment at any given moment and what capability the system has with regard to extinguishing fires.

3.2 CAD

To enable the creation of a simulation model, 3D CAD models of the geometries of interest were needed. To create these CAD models, the software Catia V5 was used.

3.2.1 Bottle and Piping System

The geometry for the bottle and piping system was derived from the study performed by Elliott et al. [24]. For simplicity, an assumption was made that the bottle could be a sphere instead of a capsule, since there were not enough geometrical parameters given to recreate a capsule shaped bottle. A schematic representing the bottle and piping system can be seen in Figure 3.1. The bottle features a radius of 96.5 mm, the pipe a radius of 14.6 mm and the nozzle a radius of 10.7 mm.

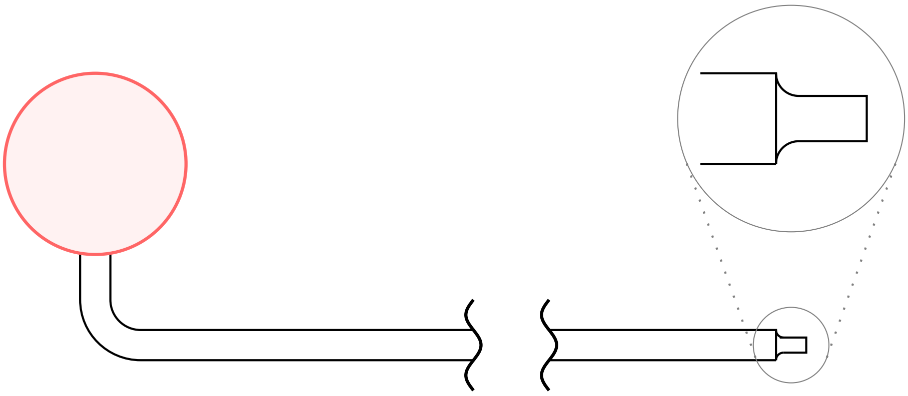

Figure 3.1: *Schematic illustrating the bottle (red), piping and nozzle (black) of the fire extinguishing system, with magnification demonstrating nozzle geometry. Note that the components are not shown in the same scale.*

3.2.2 Cargo Compartment

In order to set up the simulation of the cargo compartment, a CAD geometry of the cargo compartment was necessary. A CAD model was obtained from the interior department at Heart Aerospace, which was used as the basis for recreating a separate representative generic geometry. The final design of the cargo compartment was not frozen at the time of writing this report, therefore the geometry may be modified in the future.

After receiving the CAD model of interest, minor modifications were carried out to make the geometry as similar to the simulation case as possible. This pre-processing process takes place in the form of model preparations of the CAD model before CFD simulation. Among other things, a door sealing was added to better represent the reality where an air leakage in the compartment might be present. From conversation with a fire protection systems engineer, it was stated that based on previous experiences, it would be more conservative to consider a maximum leakage rate (in flight conditions) of around 1000 cubic feet per hour. This estimate is based on the internal volume of the current cargo compartment design and is approximately equal to 9.3 g/s. The door sealing had a width of 5 mm, since anything smaller might be problematic when preparing the CFD mesh and boundary conditions.

Two holes were made in the ceiling to represent the discharge nozzles in the firex system. The reason why there are two nozzles is based on experience of the company. The ceiling had also been slightly modified, from round to flat, to take into consideration the space of wires and cables that will be located there in the final design. To simplify the simulation work in terms of meshing, boundary conditions and pre-processing, the CAD model geometry was divided into relevant parts and named accordingly. The geometry was mainly divided into linings, door sealing and inlets. The CAD model representing the cargo compartment used for simulation is shown in Figure 3.2.

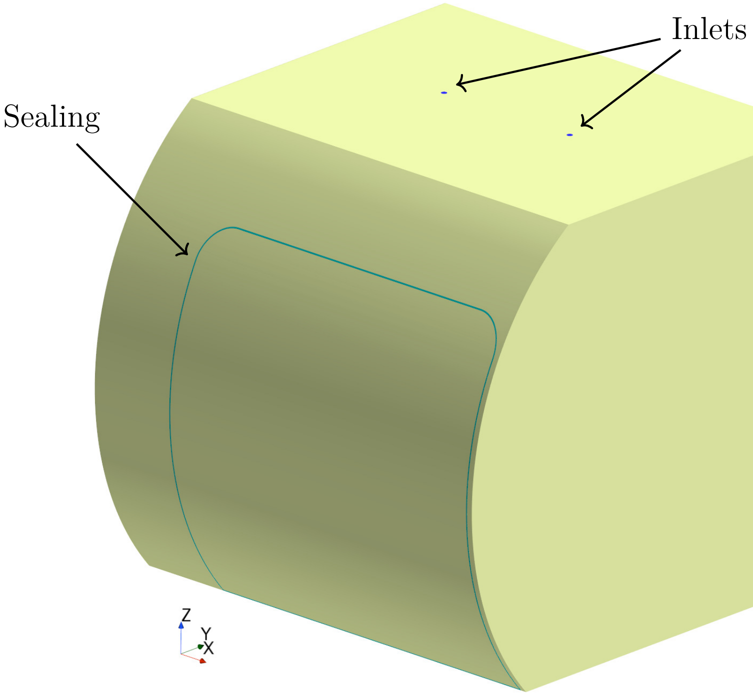

Figure 3.2: *CAD model of the cargo compartment. Linings (yellow), door sealing (green) and inlets (blue). The door sealing and inlets are marked with arrows.*

3.3 CFD

Simcenter Star-CCM+ was used for simulation of both the bottle and piping system, as well as the cargo compartment. This section contains the mesh preparations and setups for the two simulations.

3.3.1 Bottle and Piping System

Below, the method for setting up the mesh and physics models for the bottle and piping system is described.

3.3.1.1 Mesh Generation

The mesh structure of the bottle consisted of a surface wrapper and polyhedral mesher.

For the piping, two mesh strategies were evaluated. The first method involved a directed mesher, with a conformal interface from the polyhedral meshed start of pipe. Directed meshing allows the cells to be aligned with the flow direction, which should reduce numerical diffusion. It also allows for some slight cell stretching when the pipe flow is fully developed, which allows for a reduction in cell count. The second strategy included the piping in the same polyhedral meshing operation as bottle, resulting in a polyhedral volume mesh for the pipe too.

The first step of the meshing process was importing the CAD geometry into Star-CCM+. Thereafter, the bottle and pipe are treated differently. The bottle, which includes a small stub of the pipe, was meshed first using the automated meshing operation. The volume mesh was of an unstructured polyhedral type, which uses an arbitrary polyhedral shape for each cell. It is in the same meshing operation that the prismatic layers may be created, since the polyhedral mesh is built upon them.

The prismatic layers were implemented in order to accurately resolve the boundary layer. Since the $k-\varepsilon$ model was implemented together with an “All y^+ treatment” model, prism layer settings were chosen such that either $y^+ \leq 1$ or $30 \leq y^+ \leq 200$ was fulfilled. Initially, the settings used were derived from pipe flow theory. Some tuning of the settings resulted in y^+ values mainly below $y^+ < 1$ along the surface. In some instances, cells close to the bend would find values of $100 \leq y^+ \leq 200$, but this is acceptable since the “All y^+ treatment” model was applied. The exact reason for the inconsistency was unclear, as it did not correlate with the movement of neither nitrogen or Halon. Occasionally a few cells would even spike above $y^+ >$ 200, although this only seemed to occur near the outlet. The reason for this is probably due to the high velocities and pressures experienced at the nozzle outlet. Technically these peak values are not preferred, but are considered manageable for this simulation case.

Then, the directed mesher operation was used to sweep the end face of the meshed pipe stub along the pipe direction. This ensures a conformal interface between the two separately meshed parts, which eases calculation of mass fluxes between cell faces at the interface. Since the prism layers created by the automated mesh are also present on the interface, they were automatically extruded along the pipe, ensuring the same prism layer conditions. Another advantage of the directed mesher is, as previously mentioned, the reduction of numerical diffusion, due to the cells aligning with the flow direction. However, after some test simulations, the directed mesh method was not applied and was replaced by only using the polyhedral mesher.

In Table 3.1, the settings used for the volume mesh and directed mesh can be found. Figure 3.3 shows parts of the resulting mesh.

Table 3.1: *Settings used for volume- and directed mesh of bottle and piping system in Star-CCM+.*

	Volume mesh	Directed mesh
Base size	50 mm	50 mm
Target surface size	75% (37.5 mm)	75% (37.5 mm)
Minimum surface size	2% (1 mm)	2% (1 mm)
Number of Layers (Volume Extruder)	-	100
Stretching (Volume Extruder)	-	Two Sided Hyperbolic 0.5mm at source 1.0mm at target
Number of prism layers	8	8
Prism Layer Stretching	1.44	1.44
Prism Layer Total Thickness	1 mm	1 mm

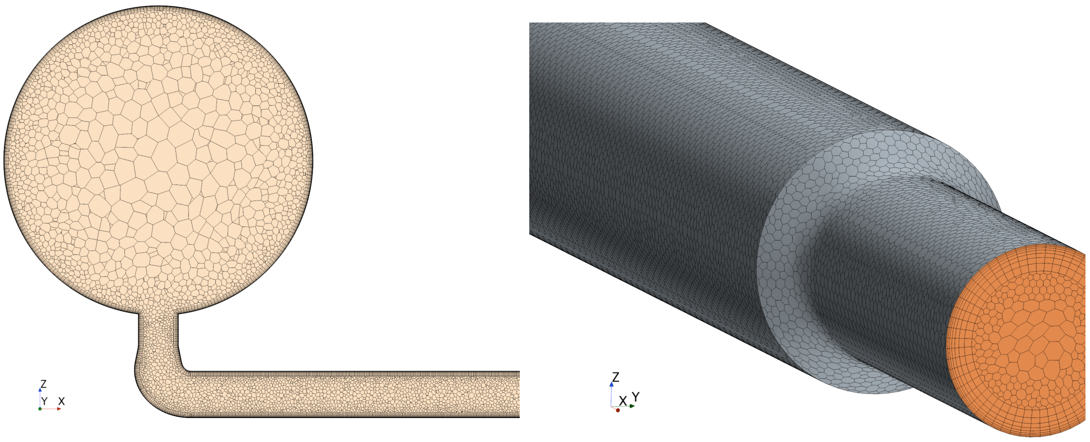

(a) *Mesh at Y=0, showing a section through bottle and part of piping.* **(b)** *3D view of mesh, showing nozzle and part of piping.*

Figure 3.3: *Visualisation of mesh with a section through the bottle and part of the pipe, and a 3D view of the nozzle.*

3.3.1.2 Physics Models

To model the two-phase flow problem of the piping, an implicit unsteady RANS model was chosen, together with VOF to track the two phases. For the turbulence model, $k-\varepsilon$ was chosen. Typically for flows largely influenced by walls, as is the case for the piping, SST $k-\omega$ is chosen. However, it is less stable compared to $k-\varepsilon$. Using the SST $k-\omega$ model was attempted, but it was eventually neglected as part of troubleshooting the overall instability of the model. In order to perform transient analysis of turbulent flow, a segregated pressure-velocity solver is required in Star-CCM+.

The two phases treated in the model were gas and liquid, for nitrogen and Halon respectively. The nitrogen was treated as an ideal gas and Halon as a mildly compressible fluid. The equation of state for Halon was user-defined as in Equation 3.1, after personal communication with Siemens support.

$$\rho = \rho_0 + p\frac{d\rho}{dp} \tag{3.1}$$

All the selected models for the piping system can be found in Table 3.2.

Table 3.2: *Physics models used for bottle and piping system in Star-CCM+.*

Physics Models
Adaptive Time-Step
Multiphase
Eulerian Phases: N_2 & Halon 1301
Volume of Fluid
Implicit Unsteady
Turbulent
$k-\epsilon$ Turbulence
Realizable $k-\epsilon$ Two-Layer Wall Treatment
Reynolds-Averaged Navier-Stokes
Two-Layer All $y+$ Wall Treatment
Segregated Flow
Segregated Fluid Isothermal
Gradients
Solution Interpolation
Three Dimensional
Wall Distance

3.3.1.3 Initial and Boundary Conditions

Apart from the boundary condition “wall”, there was only one boundary condition applied, namely the pressure outlet. However, the implementation of the pressure boundary was not as trivial as prescribing a value for atmospheric pressure. The domain was initialised with a pressure of 5.2 MPa, according to the experimental setup used in the study by Elliott et al. [24]. Due to the high initial pressure, it was good practice to initiate the pressure boundary with the same pressure as the rest of the domain. The pressure boundary can then be ramped down to an atmospheric value after a certain duration. Ramping the pressure decreases the likelihood of divergence, as it becomes easier for the numerics to treat the pressure gradient. The function used to ramp the pressure is given in Equation 3.2, where $g(t)$ is then multiplied with the initial pressure in order to bring down the pressure applied at the boundary. The resulting field function is plotted in Figure 3.4.

$$g(t) = \begin{cases} \cos\left(\frac{\pi t}{0.1}\right) + 0.5 & t < 0.1\text{s} \\ 0 & t > 0.1\text{s} \end{cases} \tag{3.2}$$

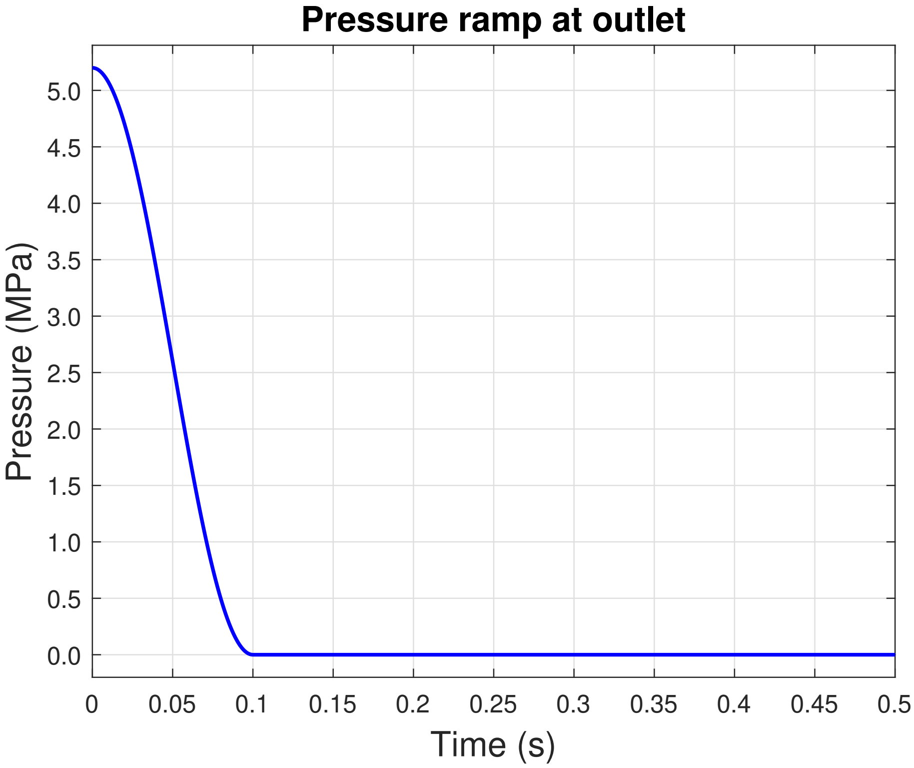

Figure 3.4: *Plotted field function g(t) ramping the pressure at the nozzle outlet.*

To prescribe the initial amount of Halon, a user-defined field function for the initial volume fraction was created in Star-CCM+. The field function provides a scalar between 0 and 1, where 1 implies the presence of Halon. For the volume fraction of nitrogen, it is as simple as defining that everywhere Halon is present, the nitrogen is not. So, if the volume fraction of Halon is given as α_{Halon}, then the volume fraction of nitrogen is found as $\alpha_{N_2} = 1 - \alpha_{Halon}$. It was then left to decide which part of the domain should be initialised with Halon, which is given from the study conducted by Elliott et al. [24].

From the same study, the bottle volume and mass of Halon fill was known, which was enough to derive for which cell positions Halon should be present. Due to Halon being more dense than nitrogen, the Halon occupies the bottom of the sphere, creating a spherical cap. In Equation 3.3, the volume of a spherical cap is described, where R is the radius of the sphere and h the height of the cap. The volume V_{cap} is found by taking filling mass over density, only leaving h unknown. By solving for h, it was possible to define for which positions along the Z-axis the bottle should be filled, automatically filling every cell along X and Y respectively. Figure 3.5 visualises the spherical cap.

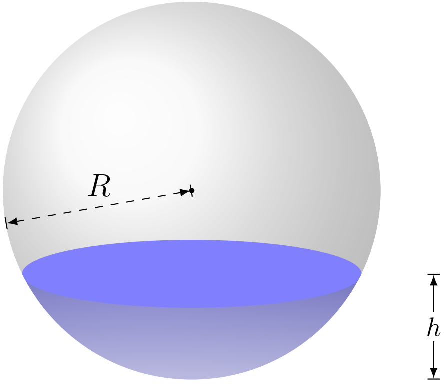

Figure 3.5: *Sphere of radius R with spherical cap of height h, representing the filling volume of Halon.*

$$V_{cap} = \frac{1}{3}\pi h^2(3R - h) \tag{3.3}$$

Table 3.3: *Initial conditions used for the bottle and piping in Star-CCM+.*

Initial Condition	**Value**
Pressure	5.2 MPa
Temperature	20 °C

Table 3.4: *Boundary conditions used for the bottle and piping in Star-CCM+.*

Boundary	**Boundary Condition**	**Value**
Nozzle	Pressure outlet	0 Pa
Bottle	Wall	No-slip
Pipe	Wall	No-slip

3.3.1.4 Solver Settings

To further increase the stability of the simulation, an adaptive time step was adopted. When dealing with large pressure gradients, too large of a time step can affect the numerical stability. Although, it was not as simple as only altering the time step. Often the Courant-Friedrichs-Lewy (CFL) condition is mentioned, which relates the time step to the mesh size. The condition expresses that the distance information travels within a time step must not exceed the distance between mesh elements [25], [26]. Ideally, for every time step, information should only propagate from one cell to adjacent cells. If not fulfilled, the numerical solution may deviate in accuracy or even diverge towards infinity.

However, when adopting a small time step it is unnecessary to always use a small step when the pressure drop decreases and becomes easier to solve for. Therefore it is advantageous to use an adaptive time step, which allows the simulation to automatically increase or decrease the time step.

The adaptive time step setting allowed for a selection of the amount of iterations per time step, referred to as inner iterations. The number of inner iterations were allowed to vary, with a minimum of 5 and a maximum of 100. For the earliest stages of the simulation when the pressure gradients are the largest, more inner iterations were required to achieve convergence. However, when the simulation reached a more stable state, the solving time was decreased as fewer inner iterations were required.

In order for the solver to assess convergence and progress to the next time step of the simulation, a few different stopping criteria were used. The stopping criteria were based on monitors, which observe properties such as pressure, velocity and mass. Using an asymptotic criterion, the solver samples values from the monitors, allowing progression to the next time step once the values stabilise and only vary within a certain range for each new inner iteration.

3.3.2 Cargo Compartment

Below, the creation of the mesh and the physical models used for the simulation of the cargo compartment are presented. Once the model was created, the settings were reused for running a set of simulations with varying nozzle conditions.

3.3.2.1 Mesh Generation

Before setting up the simulation of the cargo compartment, pre-processing of the model was executed. To simplify the meshing of the geometry, a surface wrapper was created to avoid possible surface repairs in terms of intersections and gaps. In Table 3.5, the settings used for the surface wrapper are found.

Table 3.5: *Settings used for surface wrapper of cargo compartment in Star-CCM+.*

	Surface wrapper
Base size	32 mm
Target surface size	25% (8 mm)
Minimum surface size	8% (2.56 mm)

An automated volume mesh was then executed on the surface wrapper volume. The volume mesh consisted of a polyhedral mesh with prism layers at the walls. The settings used for the volume mesh of the cargo compartment are found in Table 3.6.

Table 3.6: *Settings used for volume mesh of cargo compartment in Star-CCM+.*

	Volume mesh
Base size	10 mm
Target surface size	50% (5 mm)
Minimum surface size	10% (1 mm)
Maximum tet size	20 mm
Number of prism layers	8
Prism layer growth ratio	1.32
Prism layer total thickness	2.75 mm

With the above mesh settings, the mesh quality diagnostics were investigated. The mesh quality was summarized in a couple of valuable parameters such as cell quality, face validity, volume change and skewness angle. Cell quality is a metric where 1 indicated a good quality mesh, while approaching 0 is considered bad. For face validity, 1 indicates a good quality while below 0.5 is poor. Volume change is a metric that evaluates the change of cell volume between adjacent cells and, according to guidelines, must be greater than or equal to 0.01. Investigation of the quality of the mesh used for the cargo compartment simulation showed overall high cell quality and face validity together with volume change. The final metric used to study the quality of the mesh was skewness angle. This metric is used to study the angle distribution among the cells, where an angle of zero degrees means that the faces of the cells are orthogonal to each other - which is desirable. Guidelines recommend that the skewness angle should be less than 85 degrees to ensure good mesh quality. The skewness angles of the overall mesh were concluded sufficiently low. Apart from the metrics described above, the absence of negative volume cells were ensured. This is a requirement that must be met to even consider the mesh as acceptable [27].

The mesh consisted of prism layers and, more specifically, it consisted of 8 prism layers. The mesh had a prism layer growth ratio of 1.32 to avoid expanding the prism layer cells too quickly. The prism layer growth ratio is a trade-off between the number of prism cells and computational storage. When generating a prism layer mesh, it is not unusual for the mesh quality to deteriorate locally around corners or narrow gaps. This is commonly referred to as layer reduction. In order to counteract layer reduction in the corners of a mesh, the number of prism layers is kept as low as possible while considering the requirements for capturing flow near the wall. The mesh with and without layer reduction can be visualized in Figure 3.6a and Figure 3.6b, where the latter is the mesh that was continued with.

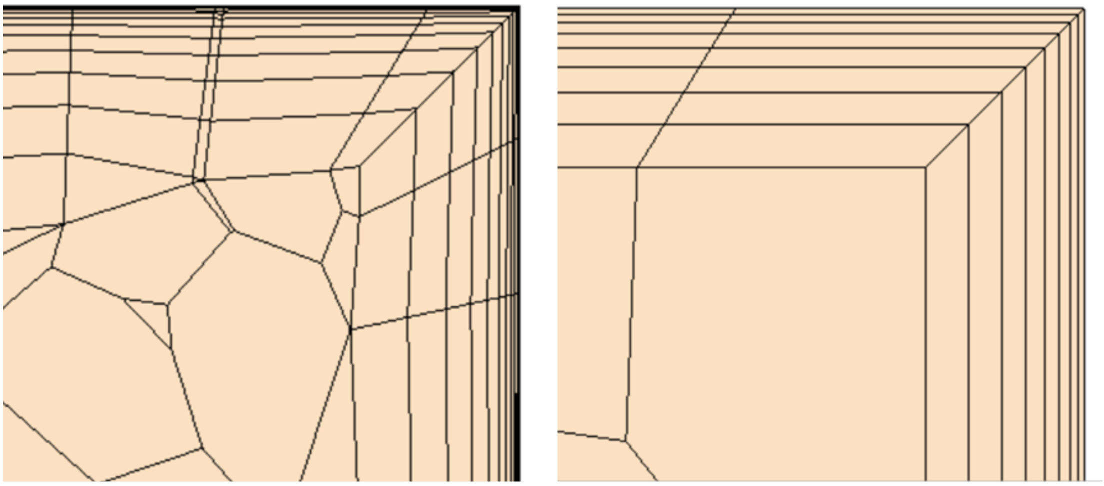

(a) *Corner of meshed domain at Y=0 with prism layer reduction.*

(b) *Corner of meshed domain at Y=0 without prism layer reduction.*

Figure 3.6: *Comparison of meshes with and without prism layer reduction.*

The mesh had also been locally refined in some critical areas such as the door sealing and the nozzles. Since the door sealing is such a small volume, more cells were needed there to capture the leakage flow with associated pressure and velocity gradients expected to occur in that region. The number of cells was thus increased by locally adding surface controllers. Locally finer mesh was also made using volumetric controls, for the same reason as mentioned earlier, to capture the critical flow entering the cargo compartment through the nozzles. These volumetric controls were applied as two cylinders created around the two nozzle openings located in the ceiling of the cargo compartment. The height distance of the volumetric controls were considered reasonable, given the expected flow in this part of the compartment. The volumetric controls around the nozzles can be seen in Figure 3.7a, while the resulting finer mesh in this area is seen in Figure 3.7b. All these mesh settings result in a total cell count of approximately 12 million cells.

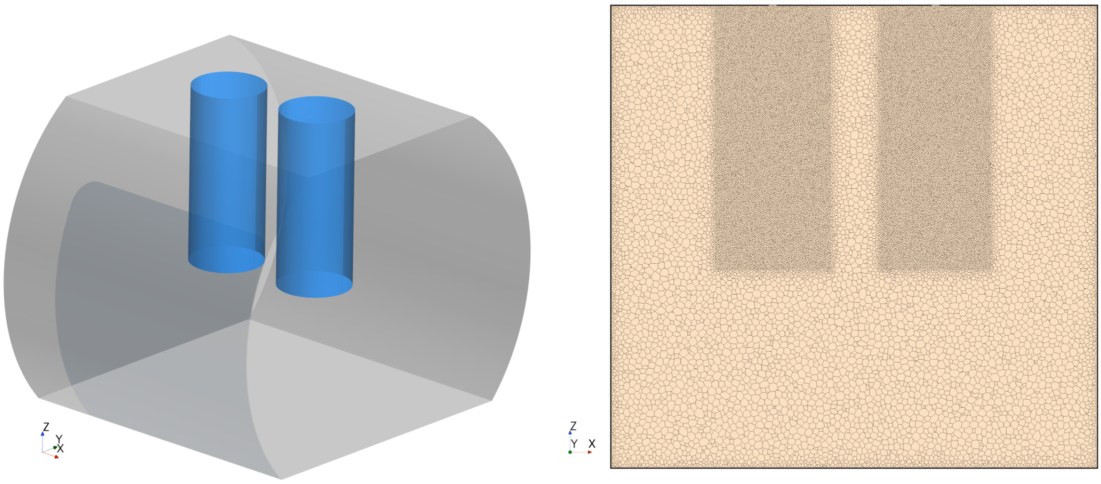

(a) *Volumetric control regions (blue) spaced concentrically to nozzle inlet.*

(b) *Mesh at Y=0 with visible local refinements around nozzles and along expected flow direction, as a result of the volumetric controls.*

Figure 3.7: *Visualisation of the cylinders used for volumetric controls together with the resulting mesh refinement.*

Using these mesh settings resulted in good y^+ values for the chosen wall treatment model. The y^+ values after 0.1 seconds of simulation can be seen in Figure 3.8. As seen in Figure 3.8, the highest y^+ values were observed around the door sealing and inlet nozzles, which was expected given the high pressures and velocity gradients experienced in this region. The flow is not completely parallel to these surfaces either, changing the conditions for boundary layer formation. All other walls in the cargo compartment were zero, which is most important to ensure proper mesh size. Resulting in $y^+ < 1$ at the walls was accomplished by tuning the prism layer and mesh settings used for the model.

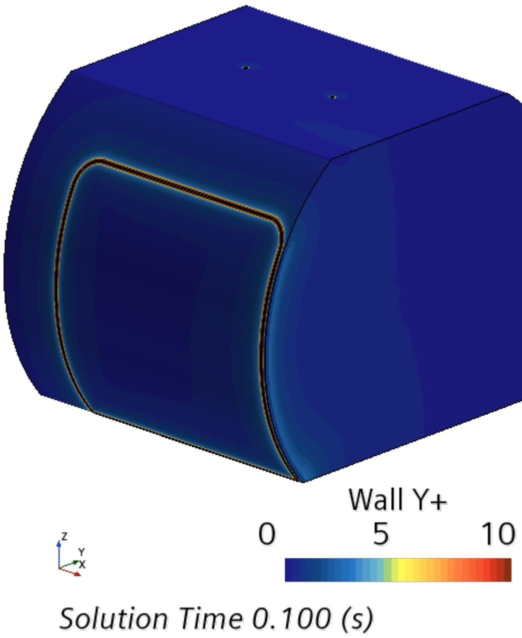

Figure 3.8: *The wall y^+ for the prism layer of the cargo compartment surfaces.*

3.3.2.2 Physics Models

Assumptions were initially made regarding the modeling of the Halon discharge. In the first simulation, the Halon was considered a liquid when entering the cargo compartment. This resulted in Star-CCM+'s MMP model being used. However, after further study of Halon behaviour and corresponding phase changes when it enters the cargo compartment, it was realized that it is mainly gas phase and, therefore, a single phase model was sufficient for the simulation of the cargo compartment.

The modeling of the Halon discharge into the air filled cargo compartment was then done using Star-CCM+'s multi component, single phase, gas model. The two gas components consequently consisted of air and Halon, both treated as ideal gases. From discussions with a fire protection systems engineer, it was decided to use a non-reacting model since it is not necessary for Halon to react directly with the air inside the compartment to be able to extinguish a fire. Instead, Halon is assumed to only chemically react with a fire present, not directly with air.

Similarly to the simulation of the bottle and piping system, the simulation of the cargo compartment used an implicit unsteady RANS solver together with the $k - \varepsilon$ turbulence model. Since the simulation flow is incompressible, it was not necessary to use the coupled flow model. Instead, the segregated flow model was used. The solver settings used in the simulation of the cargo compartment can be seen in Table 3.7.

Table 3.7: *Physics models used for cargo compartment in Star-CCM+.*

Physics Models
Multi-Component Gas
Gas Components: Air & Halon 1301
Ideal Gas
Non-reacting
Implicit Unsteady
Turbulent
$k-\epsilon$ Turbulence
Realizable $k-\epsilon$ Two-Layer Wall Treatment
Reynolds-Averaged Navier-Stokes
Two-Layer All $y+$ Wall Treatment
Segregated Flow
Segregated Fluid Temperature
Segregated Species
Gradients
Solution Interpolation
Three Dimensional
Wall Distance

3.3.2.3 Initial and Boundary Conditions

The main initial conditions for the cargo compartment simulation were initial pressure as well as density and temperature of air. The conditions under which the simulation was assumed to operate were at cruising altitude for commercial propeller airplanes, like the ES-30, that is, at an altitude of 20000 feet. At this altitude, both cabin and cargo compartment are pressurized to a pressure which enables passengers and crew members to breath comfortably. Based on these operating conditions, the pressure experienced in the cargo is 10.92 psi (equivalent to approximately 75291 Pa), which corresponds to the pressure experienced at 8000 feet altitude. At this altitude, the density of air is approximately 81% of sea level air density. The cabin air that usually recirculates in the cargo compartment is estimated to have a temperature of 20°C. Given this, the initial temperature and density of air are set accordingly. The initial conditions applied in the cargo compartment simulation are listed in Table 3.8.

Table 3.8: *Initial conditions used for the cargo compartment in Star-CCM+.*

Initial Condition	**Value**
Pressure	4.17 psi
Air density	0.975 kg/m^3
Temperature	20 °C

Where the initial pressure 4.17 psi (28751 Pa) in Star-CCM+ is relative to the reference pressure, i.e. the external pressure outside of the aircraft of 6.75 psi (46540

Pa).

The boundary conditions for the cargo compartment simulation can be seen in Table 3.9.

Table 3.9: *Boundary conditions used for the cargo compartment simulation in Star-CCM+.*

Boundary	**Boundary Condition**	**Value**
Inlets	Mass flow inlet	*f(t)* kg/s
Sealing	Pressure outlet	*g(t)* Pa
Cargo lining	Wall	No-slip

Large parts of the cargo compartment were defined as the property “wall”, with no-slip condition, meaning that the velocity at the wall is equal to zero. The parts that do not belong to the wall boundary condition were the nozzles and the door sealing. The nozzles were defined as mass flow inlets, representing the Halon being discharged into the compartment, while the door sealing was defined as a pressure outlet, representing the leakage rate out of the compartment. Where *f(t)* is a field function describing how the inlet mass flow of Halon varies over time and is given from the study by Elliott et al. presented in Section 3.1. The field function describing this phenomena can be seen in Figure 3.9.

To make the simulation more stable and avoid extreme pressure gradients, the function $g(t)$ given in Equation 3.2 was applied in a similar manner to the bottle and piping simulation.

By multiplying $g(t)$ with the initial pressure, p_{init}, the pressure experienced on the door sealing was ramped from the initial pressure experienced on the inside of the cargo (4.17 psi relative the reference pressure) down to 0 Pa gauge pressure, which corresponds to the reference pressure on the outside of the aircraft (6.75 psi). The field function is plotted in Figure 3.10.

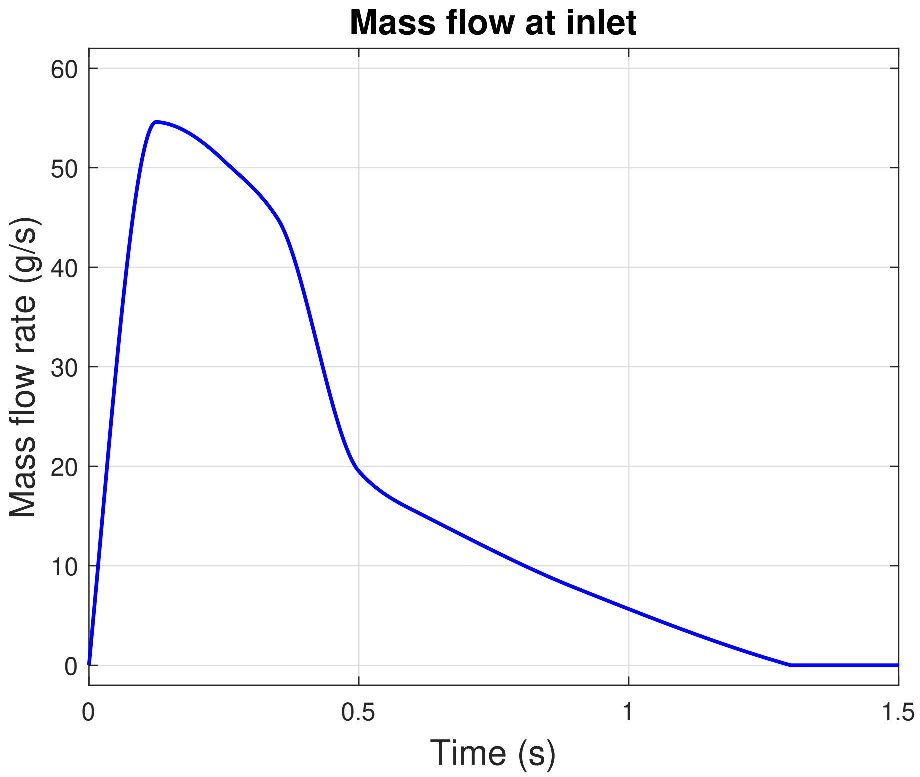

Figure 3.9: *Plotted field function f(t) describing time varying inlet mass flow used as boundary condition for the cargo compartment.*

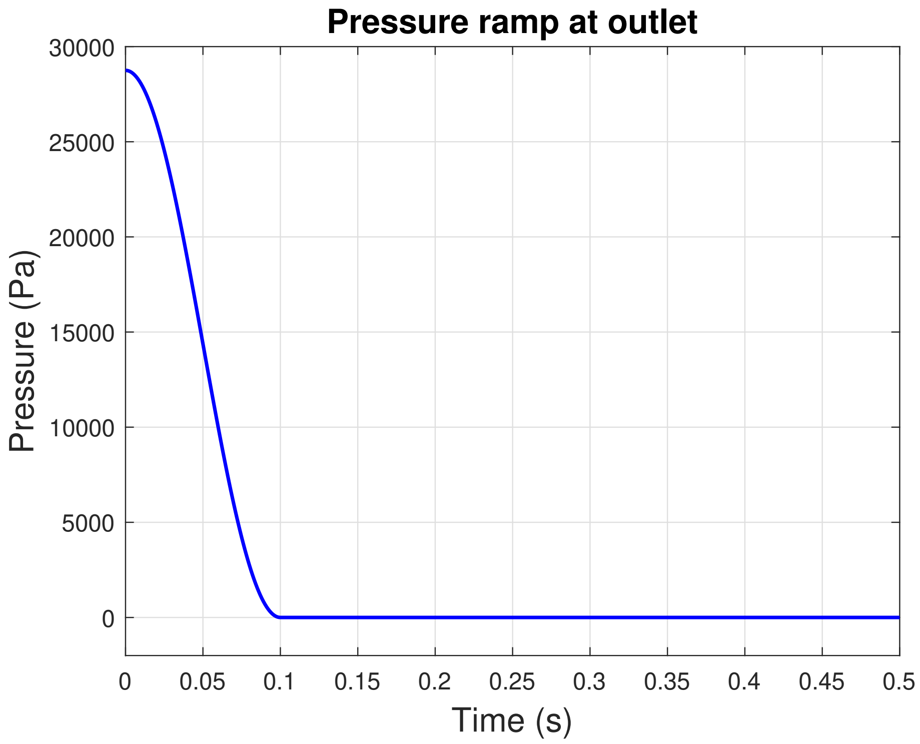

Figure 3.10: *Plotted field function g(t) ramping the pressure on the door sealing of the cargo compartment.*

3.3.2.4 Probe Distribution

As mentioned in Section 2.1.2.2, 12 probes are used in certification testing of the firex system to measure Halon concentration levels. In order to get a more comprehensive understanding of the Halon distribution, 18 probes were used in the simulation of the cargo compartment. The probe distribution, with corresponding probe positions, are visualized in Figure 3.11. The ambition with this was to be able to gain an even greater understanding of the distribution than is required during testing and thus be able to optimize the system before testing. During the CFD modeling phase, it is relatively inexpensive to add more probes than necessary, as opposed to physically adding them for testing.

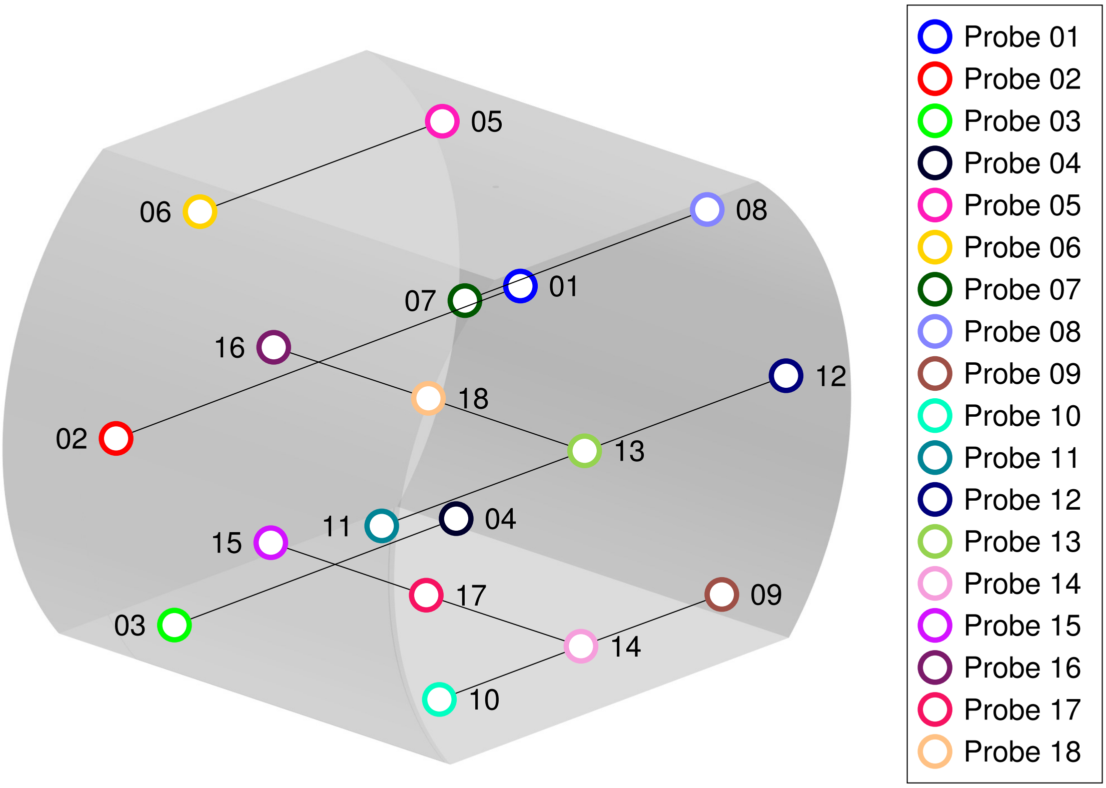

Figure 3.11: *Placement of probes measuring Halon concentration, numbered accordingly, together with lines demonstrating which plane the probes lay on.*

3.3.2.5 Mesh Study

A mesh independence study was performed to assure that the results of the simulation are not affected by changing the mesh. Due to time limitations, the mesh study was limited to four different mesh sizes. The mesh parameters adjusted between the different meshes were the base size, target surface size and maximum tet size. Importantly, the prismatic layers were left unchanged in the mesh study, since they are mainly derived from wall theory. The difference between these parameters as well as the resulting total amount of cells, are presented in Table 3.10.

Table 3.10: *Meshes and corresponding cell count for mesh study.*

Mesh	Base size	Target surface size	Maximum tet size	Number of cells
1	15 mm	10 mm	25 mm	6 million
2	10 mm	10 mm	20 mm	8 million
3	10 mm	5 mm	20 mm	12 million
4	7.5 mm	4 mm	10 mm	23 million

All mesh iterations were simulated for one second of physical time, mainly to save computation time. One second was also expected to be a long enough duration to observe the initial behaviour of the system. The monitor values compared between the meshes were the concentration probes located in the cargo compartment. During the relatively short physical time, most of the 18 probes will not detect concentration of Halon. After one second of simulation, there were only three probes that measured Halon concentrations: probe 14, 15 and 17. The three probes that gave results for concentration measurement were all located at the bottom of the cargo compartment, which was the expected outcome given the short simulation, prescribed mass flow and nozzle location. The concentration measurement of Halon among the different simulations, with the associated meshes, is presented in Figure 3.12, 3.13, 3.14 and 3.15.

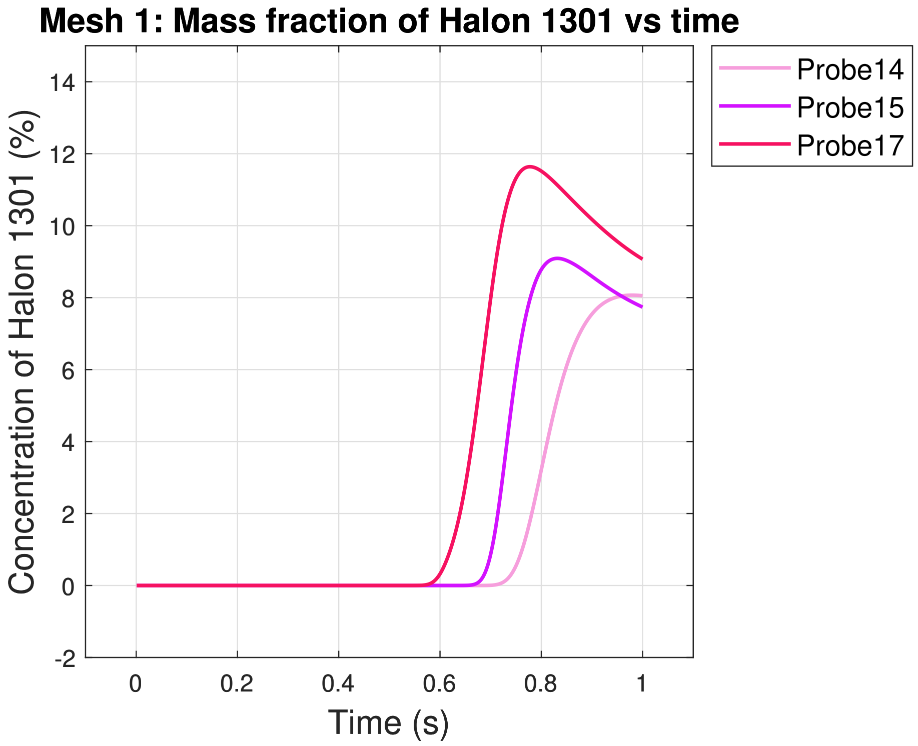

Figure 3.12: *Halon concentration measured by probes, excluding probes which did not register any concentration, for mesh consisting of 6 million cells.*

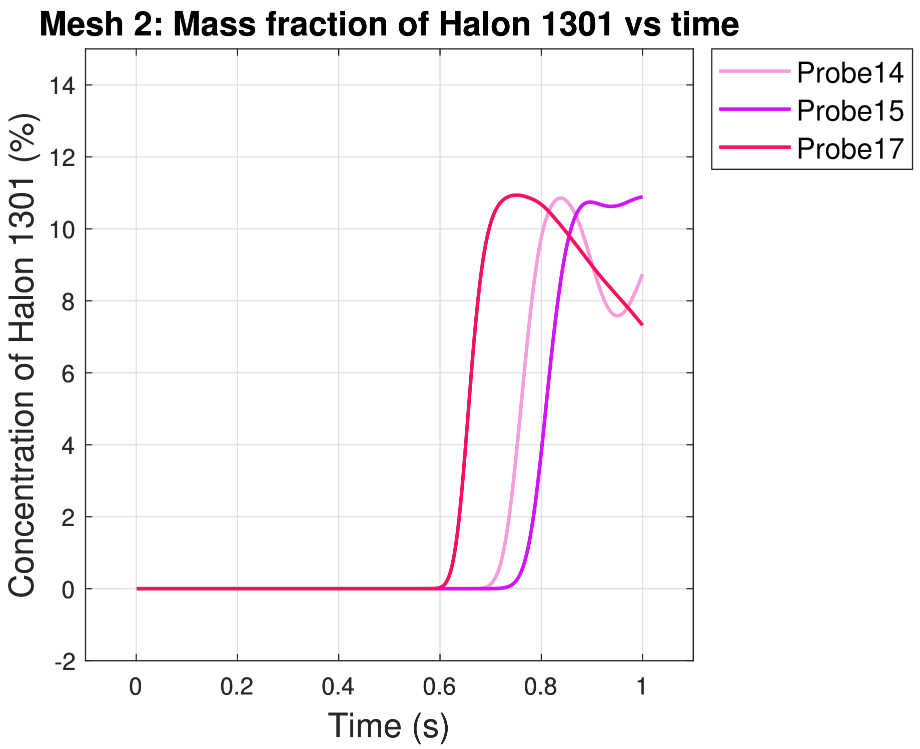

Figure 3.13: *Halon concentration measured by probes, excluding probes which did not register any concentration, for mesh consisting of 8 million cells.*

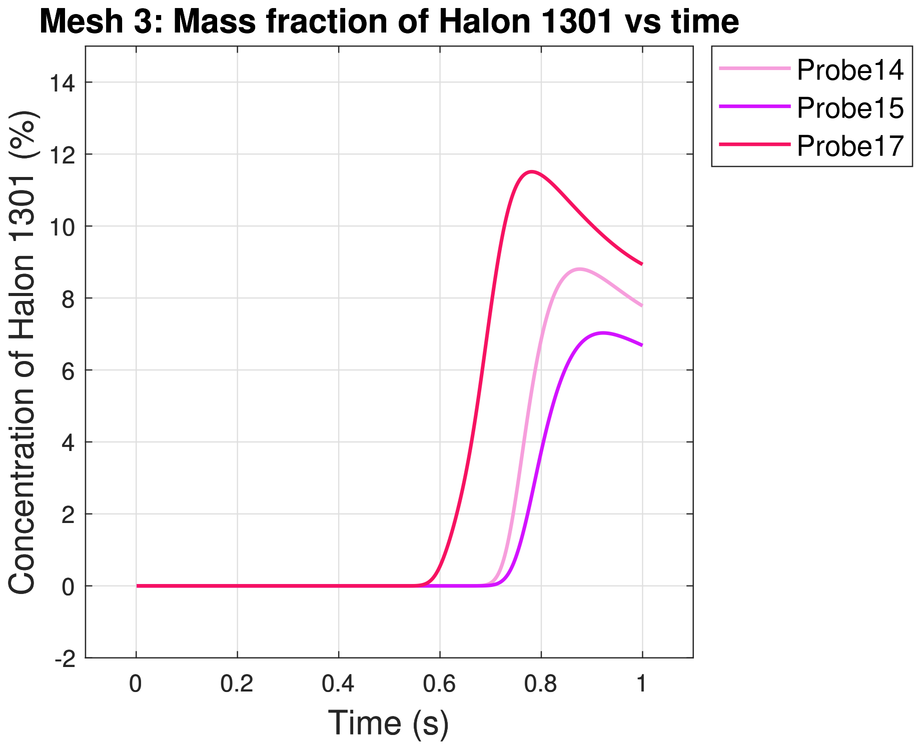

Figure 3.14: *Halon concentration measured by probes, excluding probes which did not register any concentration, for mesh consisting of 12 million cells.*

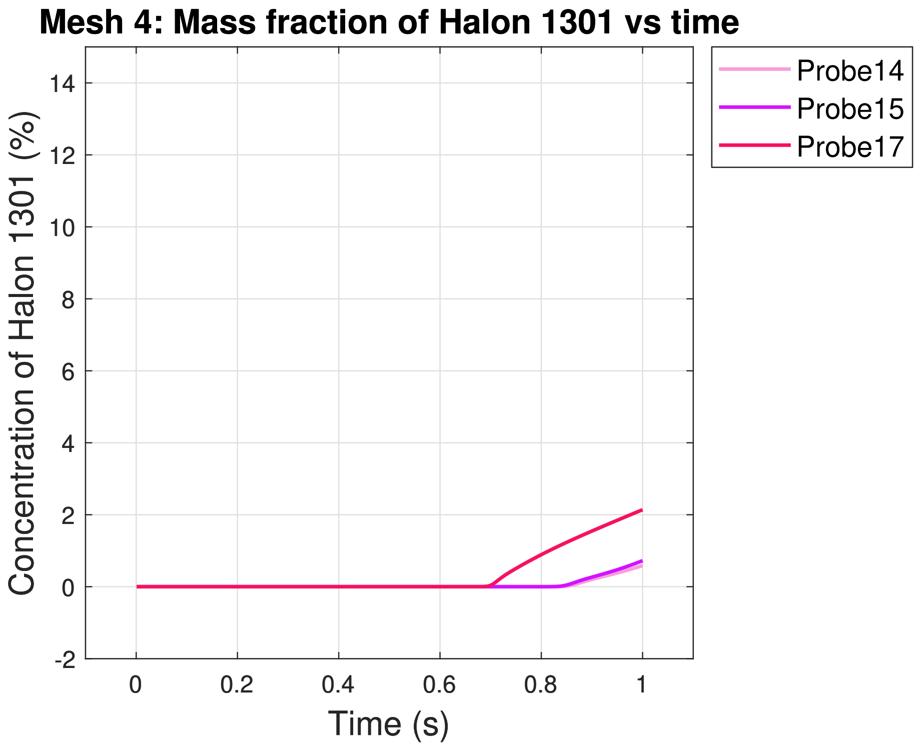

Figure 3.15: *Halon concentration measured by probes, excluding probes which did not register any concentration, for mesh consisting of 23 million cells.*

The observed concentration for the probes differs between the meshes, most notably for the finest mesh presented in Figure 3.15. For the finest mesh, mesh “4”, there were barely any readings from the probes after 1 second. For the other three meshes, probe 17 showed similar behaviour, where the Halon mass fraction for mesh “1” and mesh “3” gave identical readings. The other probes were less consistent, although mesh “1” and mesh “3” did show readings for probe 14 and probe 15 within certain magnitude. The maximum values for probe 14 differed by 0.73 percentage points, whereas probe 15 differed by 2.06 percentage points between mesh “1” and “3”.

Despite the limited mesh study performed in this thesis, it is concluded that the measured Halon concentration of the probes does not differ significantly, apart from mesh “4” which for unclear reasons does not propagate as fast. Mesh “4” also behaved unphysically, as more Halon was expected to reach the floor after 1 second. For the upcoming simulations, mesh “3” was therefore chosen, with 12 million cells, as a trade-off between solution accuracy and computational power.

4

Results & Analysis

In this chapter the results of the CFD simulations are presented and analyzed. Firstly, the results of the bottle and piping system model are presented, followed by the cargo compartment model.

4.1 Bottle and Piping System

One of the main parameters from the study by Elliot et al. [24] that may be used for comparison is the pressure inside the bottle. In Figure 4.1, the pressure drop from the simulation is presented, with experimental data from the mentioned study overlaid.

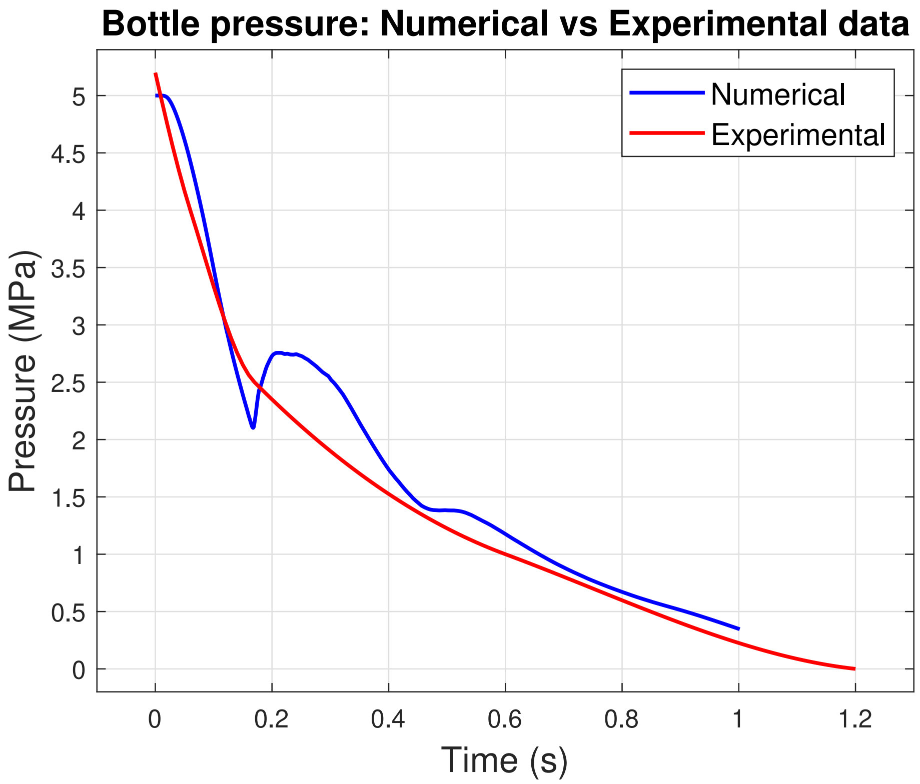

Figure 4.1: *Simulated pressure drop in bottle compared to experimental data.*

It is noted that the overall trend of the numerical data seems to match decently with the experimental data. The model slightly overestimates the pressure between

0-0.1 seconds and from 0.46 seconds to the end duration. The most inconsistent trend of the numerical data occurs between 0.17 and 0.4 seconds, where the largest deviation of 0.6 MPa is found at 0.3 seconds.

Looking at the mass flow in Figure 4.2, some questionable results can be seen. Figure 4.2a shows that the mass flow at outlet suddenly peaks after 0.12 seconds reaching a value of 78.4 kg/s. Unfortunately, the study by Eliott et al. [24] does not present the mass flow for this specific test which would help validation. However, a similar test was performed in the study, without the piping and nozzle. In this case, the mass flow peaked at 14 kg/s. Considering the change in order of magnitude, without any other experiments to prove the opposite, the large peak seems unreasonable. Figure 4.2b shows the same mass flow, while clipping the massive peak for improved readability. Excluding the largest peak, it can be seen the mass flow shows an overall increase, until the second largest peak is reached after 0.4 seconds at 6.5 kg/s.

It should be noted that the mass flow rate reported by Star-CCM+ does not seem to separate Halon from nitrogen. However, since the nitrogen is present as a gaseous phase, the mass of Nitrogen should be negligible compared to liquefied Halon.

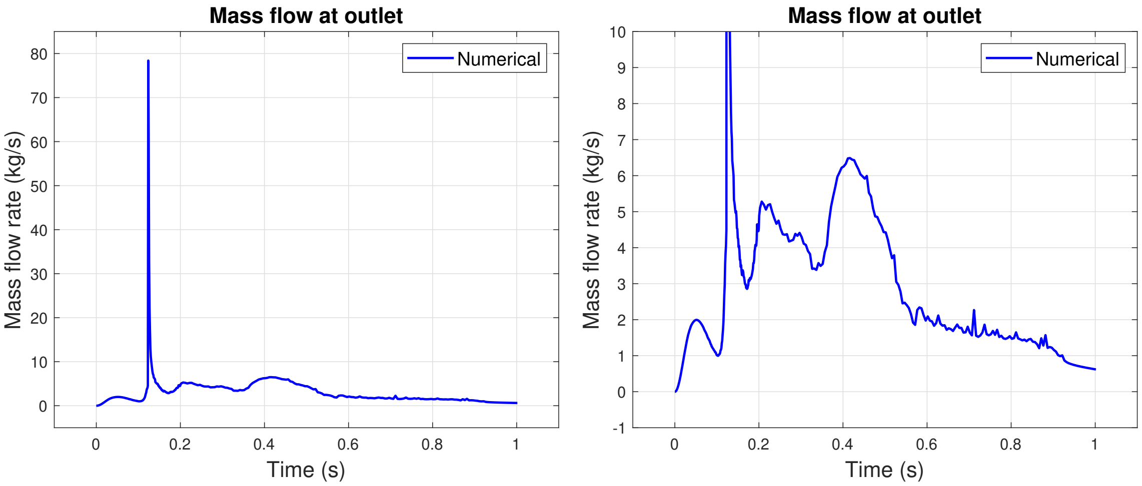

(a) *Simulated mass flow at nozzle outlet, exhibiting a large peak close to 0.1 seconds.*

(b) *Simulated mass flow at nozzle outlet, excluding the large peak for improved readability.*

Figure 4.2: *Simulated mass flow at nozzle outlet with and without clipping of large peak value.*

Figure 4.3 shows the volume fraction of Halon in the bottle, demonstrating in what manner the bottle empties. The bottle starts draining into the pipe mainly from the center, which is evident from Figure 4.3b and 4.3c. In Figure 4.3d the bottle is nearly empty, with only some Halon remaining along the walls. The remaining Halon actually stays in the bottle for the rest of the duration of the simulation.

It is possible that the choice of bottle geometry may influence how Halon drains into the pipe. If a cylinder with flat ends was used, the Halon might always remain in the corners of the bottle. Naturally, that would be detrimental to the performance of the system as less Halon would be expelled. However, the cylindrical-shaped bottles originally used in the study by Eliott et al. [24] use spherical ends, resulting in a capsule geometry. A capsule of the same volume as the sphere will have similar geometry locally to the interface between bottle and pipe, although with a smaller radius. Since the radius of a capsule is expected to be smaller, it is conceivable that less Halon might remain along the walls of the bottle, comparing to the case of a sphere.

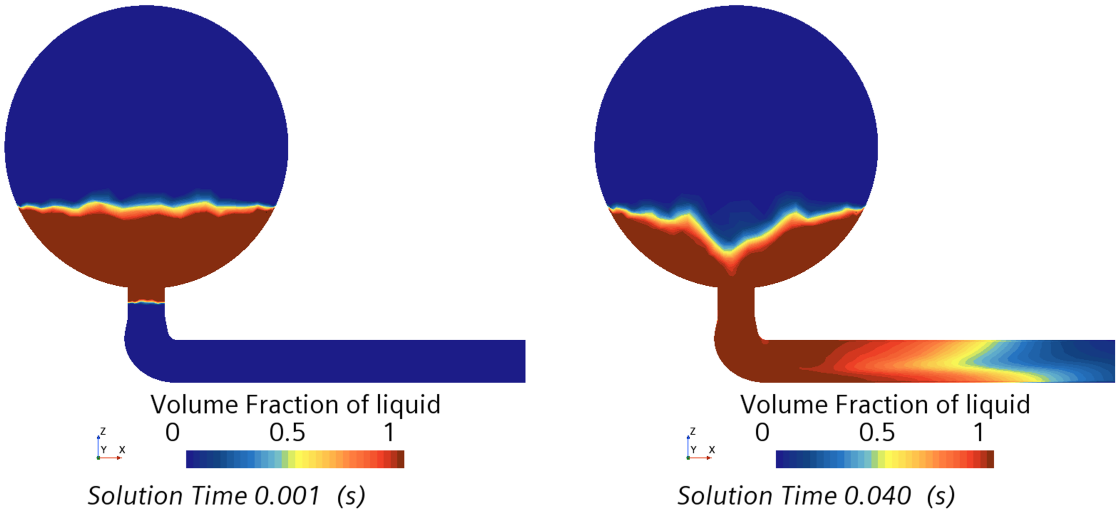

(a) *Volume fraction of Halon at Y=0 at 0.001 seconds.*

(b) *Volume fraction of Halon at Y=0 at 0.04 seconds.*

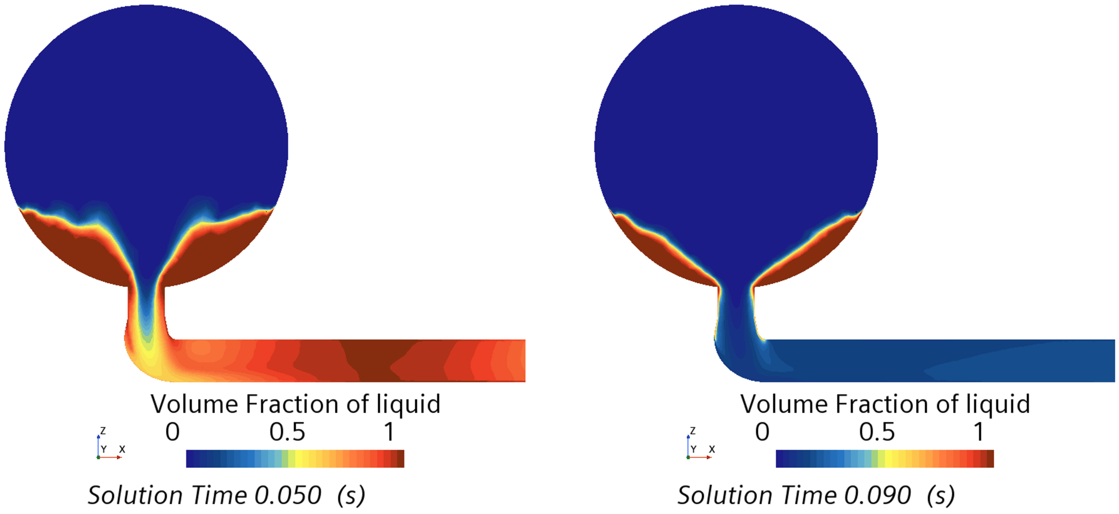

(c) *Volume fraction of Halon Y=0 at 0.05 seconds.*

(d) *Volume fraction of Halon Y=0 at 0.09 seconds.*

Figure 4.3: *Volume fractions of Halon at Y=0 after 0-0.09 seconds, demonstrating the emptying of Halon from bottle into piping.*

4.2 Cargo Compartment

For the cargo compartment, four simulation cases are executed. These cases involve both straight and angled inlet flows as well as two different angled nozzles.

4.2.1 Straight Inlet Flow

The first simulation carried out was with a straight inlet flow, i.e. Halon is released straight down into the cargo compartment. The final simulation for this case was simulated for 10 seconds, which was considered to be sufficient to replicate the first discharge. In Figure 4.4 and 4.5, the Halon distribution into the cargo compartment in terms of mass fraction is seen. When the Halon reaches the floor in the cargo compartment, it can be seen in Figure 4.4c to 4.5d how the Halon disperses, spreading the agent in the compartment.

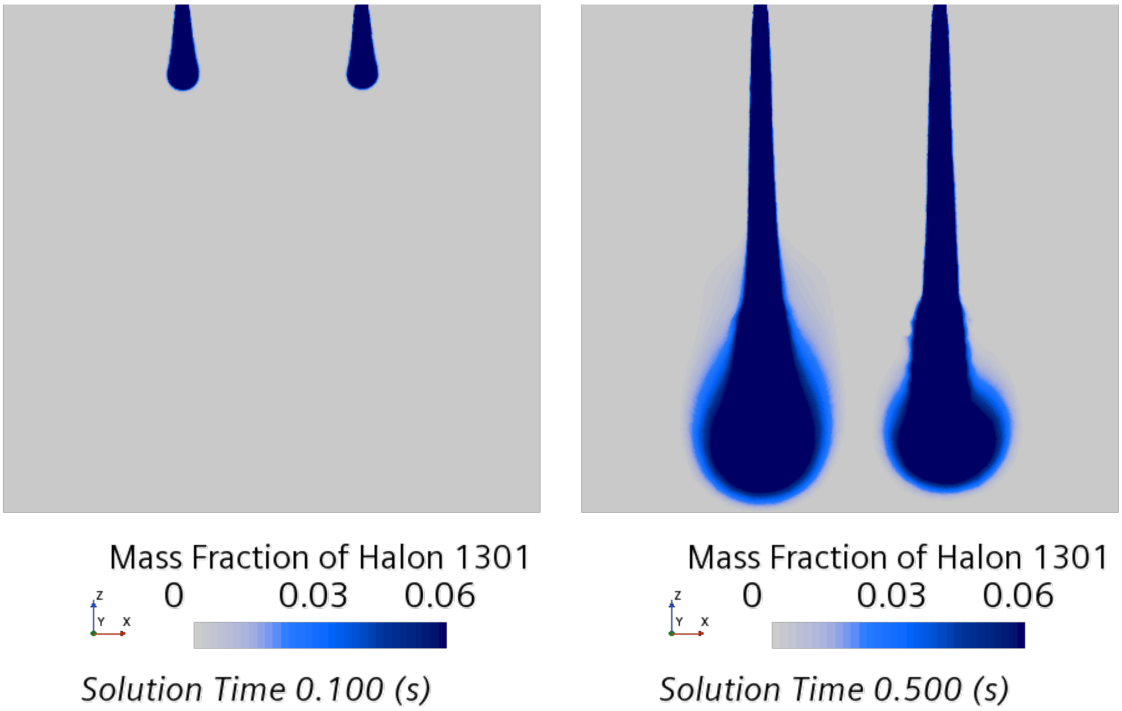

(a) *Mass fraction of Halon at Y=0 after 0.1 seconds.*

(b) *Mass fraction of Halon at Y=0 after 0.5 seconds.*

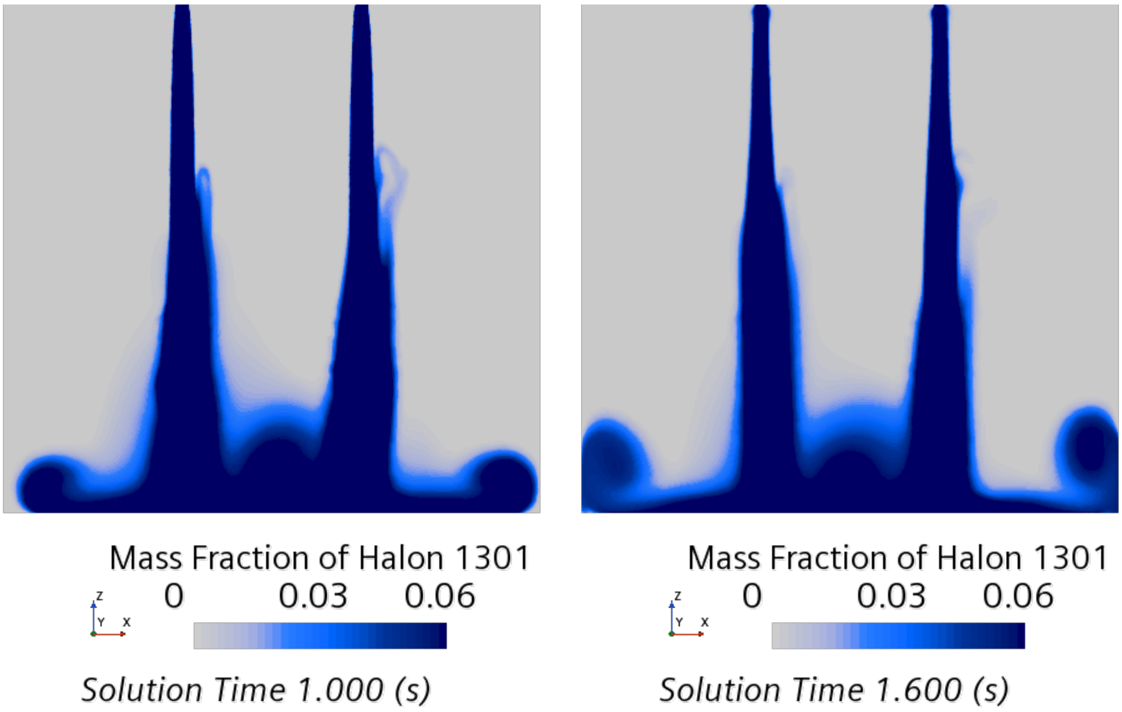

(c) *Mass fraction of Halon at Y=0 after 1 second.*

(d) *Mass fraction of Halon at Y=0 after 1.6 seconds.*

Figure 4.4: *Mass fractions of Halon for straight inlet flow at Y=0 after 0.1-1.6 seconds, demonstrating the distribution in the cargo compartment.*

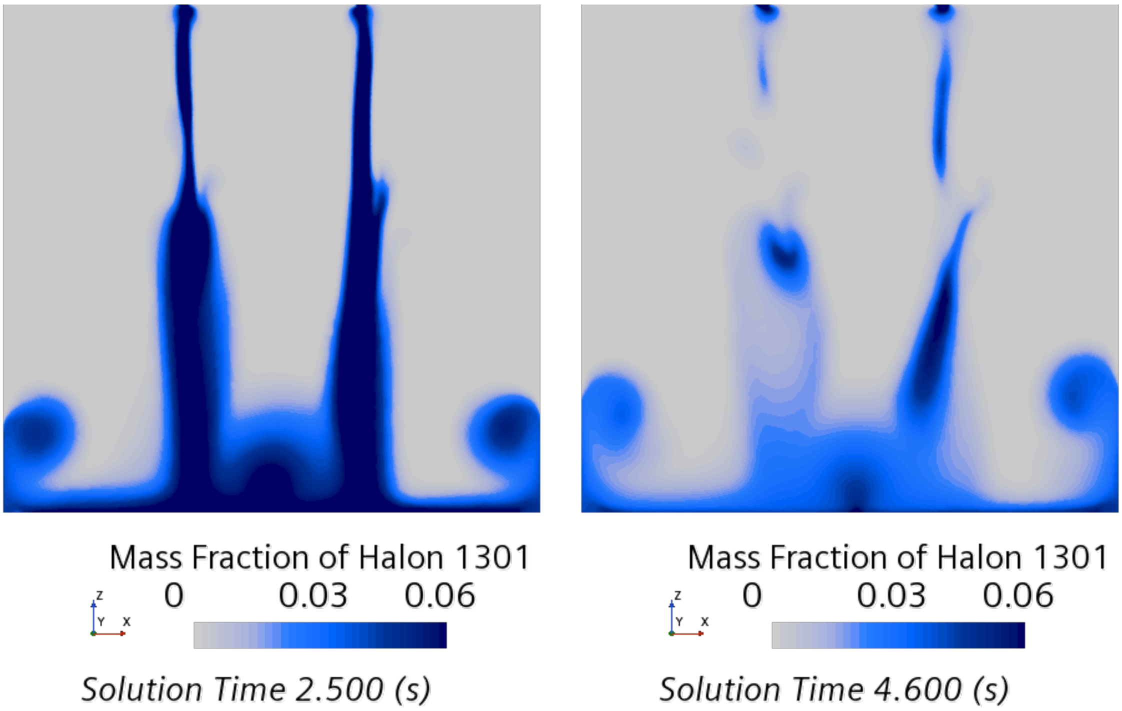

(a) *Mass fraction of Halon at Y=0 after 2.5 seconds.* **(b)** *Mass fraction of Halon at Y=0 after 4.6 seconds.*

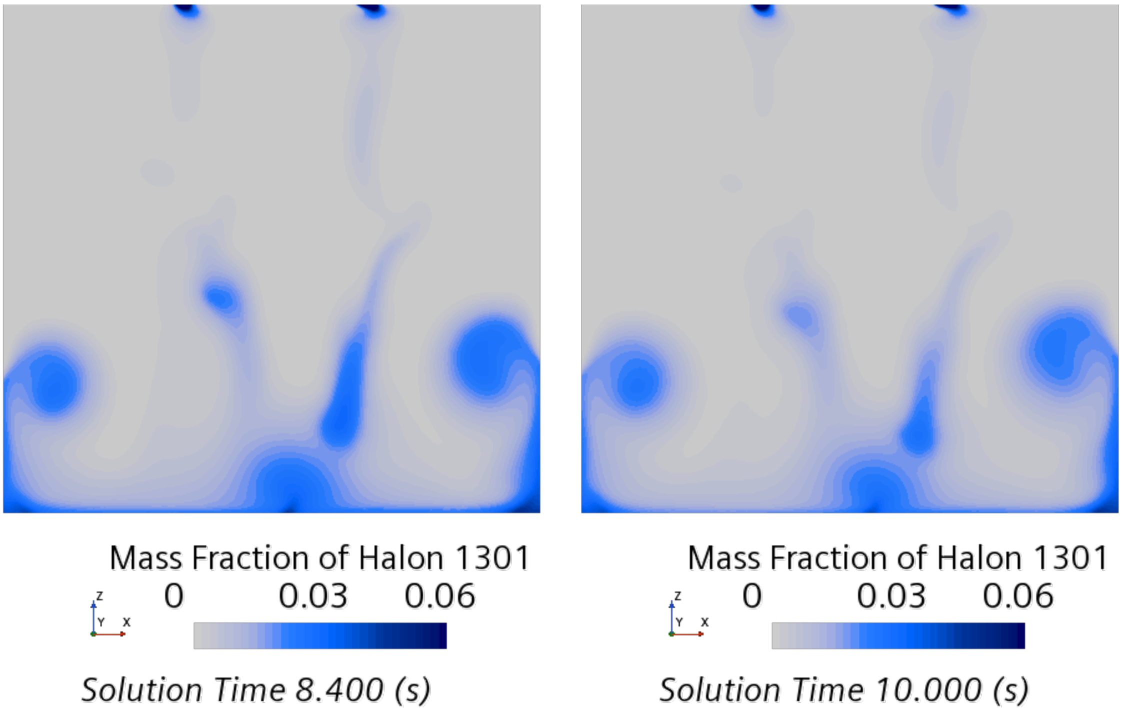

(c) *Mass fraction of Halon at Y=0 after 8.4 seconds.* **(d)** *Mass fraction of Halon at Y=0 after 10 seconds.*

Figure 4.5: *Mass fractions of Halon for straight inlet flow at Y=0 after 2.5-10 seconds, demonstrating the distribution in the cargo compartment.*

In Figure 4.6, the Halon mass fraction after 1.6 and 8.4 seconds is seen in both X- and Y-planes of the cargo compartment. Figure 4.6a to 4.6d shows a “cloud” that forms when the agent hits the floor and spreads in both height and depth.

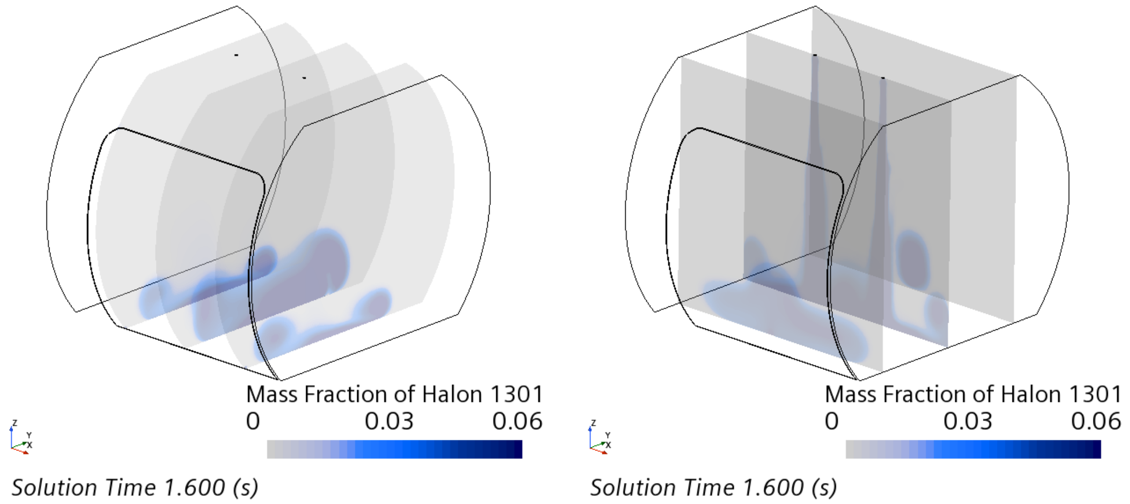

(a) *Mass fraction of Halon at 3 equidistant X-planes after 1.6 seconds.*

(b) *Mass fraction of Halon at 3 equidistant Y-planes after 1.6 seconds.*

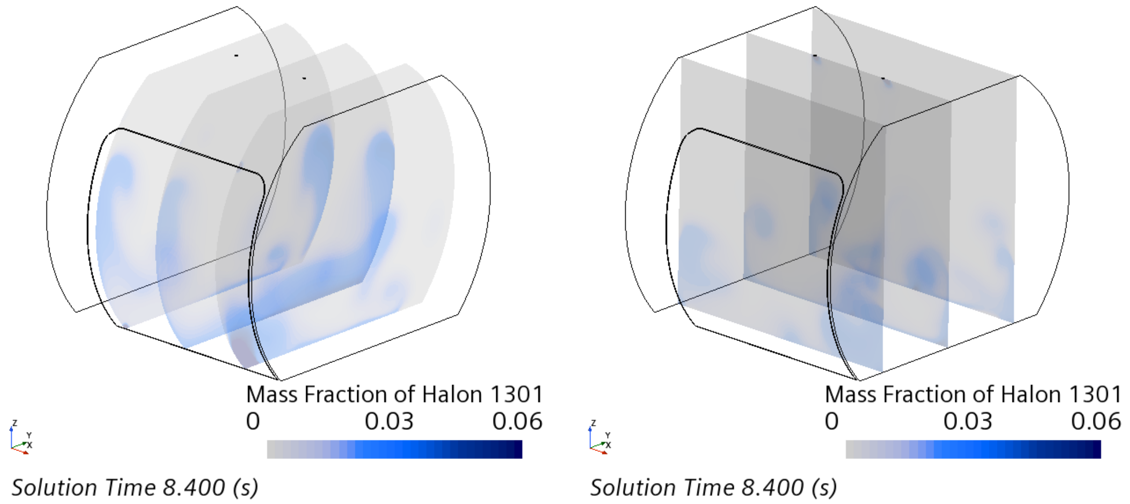

(c) *Mass fraction of Halon at 3 equidistant X-planes after 8.4 seconds.*

(d) *Mass fraction of Halon at 3 equidistant Y-planes after 8.4 seconds.*

Figure 4.6: *Mass fractions of Halon for straight inlet flow for equidistant planes normal to X- and Y-direction after 1.6 and 8.4 seconds, demonstrating the distribution in the cargo compartment.*

The probes' respective registration of Halon during the 10 seconds simulated, is reported in Figure 4.7. There are a total of 9 probes that register Halon above 0.1% concentration after 10 seconds. The probes located at the bottom of the cargo compartment, i.e. probe 14, 15 and 17, register Halon first which is expected. The concentrations measured in these probes will gradually decrease as the Halon is dispersed in the compartment. As the Halon spreads, probe 3 and 10, located closely to the front lower corners and door sealing, measure a larger concentration. The only probes reaching the required concentration of 5% in this simulation case are probe 14, 15 and 17. Probe 10 comes close, however only peaking at 4.6%. Probe 14, 15 and 17 register peak values of 8.9%, 7.0% and 11.5% respectively. The remaining probes register Halon: probe 1, 2, 3, 4 and 9, only reaches concentration peaks between 1.3-3.2% after 10 seconds of simulation, which indicates quite poor distribution.

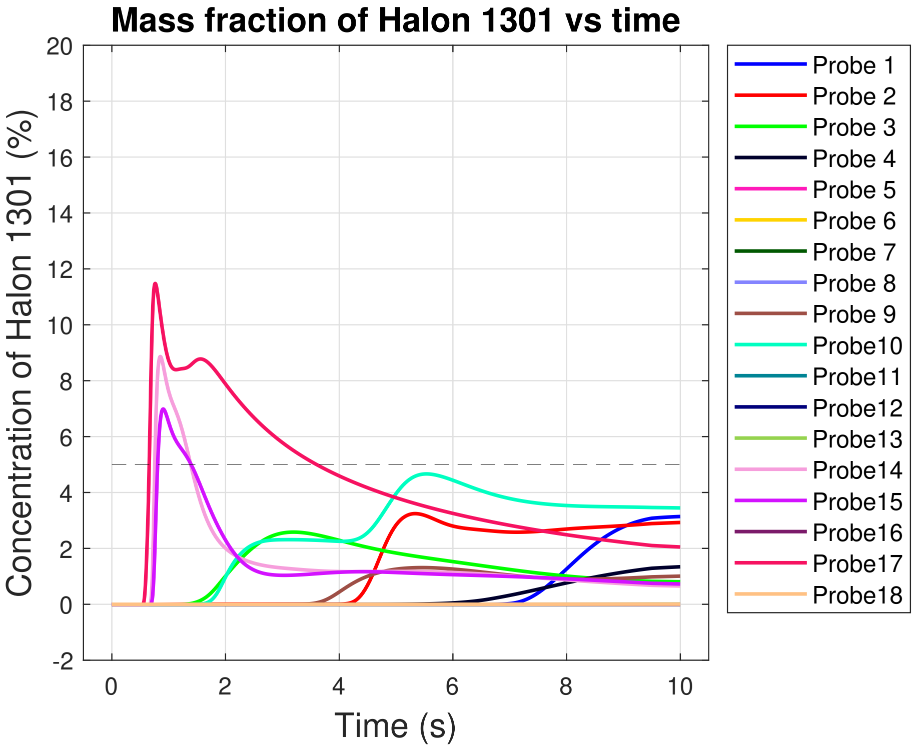

Figure 4.7: *Halon concentration measured by probes for straight inlet flow. Dashed line demonstrating the required 5% concentration level.*

4.2.2 Angled Inlet Flow and Nozzles

To investigate whether the concentration of Halon, i.e. the degree of Halon coverage, can be increased, angled inlet flow as well as nozzles are simulated. The simulations of the angled inlet flow and nozzles are simulated for 5 seconds. This is mainly a result of a trade-off between computational power and the significance of the outcome. The simulation time of 5 seconds is considered sufficient to give a first indication of how the system behaves while allowing time for several configurations to be tested.

4.2.2.1 Angled Inlet Flow

As a first simulation before the nozzles are redesigned and angled, the inlet flow is angled in direction. Instead of Halon being discharged in $(X, Y, Z) = (0, 0, -1)$ direction as in Section 4.2.1, it instead discharges in the $(0, -0.5, -0.5)$ direction resulting in a 45 degree angle relative to the original discharge. In Figure 4.8, the mass fraction of Halon is seen for some critical events of the simulation. One of the main differences is that for the angled inlet flow, the Halon bounces and rotates backwards as the flow hits the wall, i.e. earlier compared to the straight inlet flow where the backwards rotation starts when the flow hits the floor. This seems to increase the dispersion of Halon.

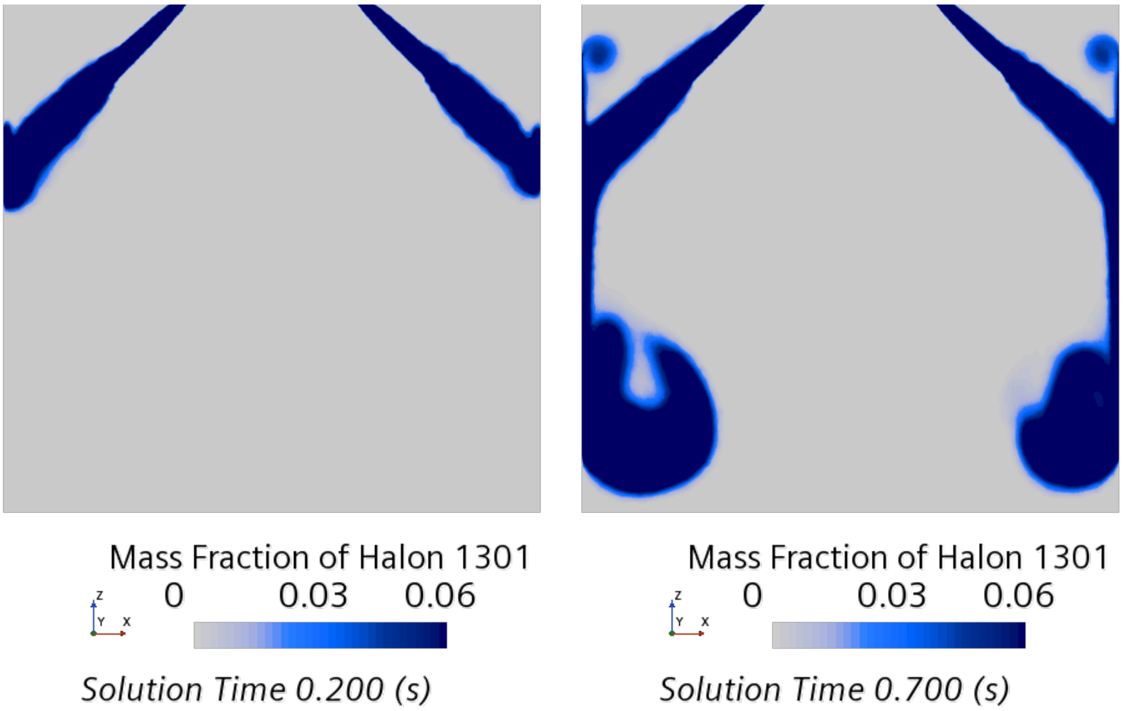

(a) *Mass fraction of Halon at Y=0 after 0.2 seconds.* **(b)** *Mass fraction of Halon at Y=0 after 0.7 seconds.*

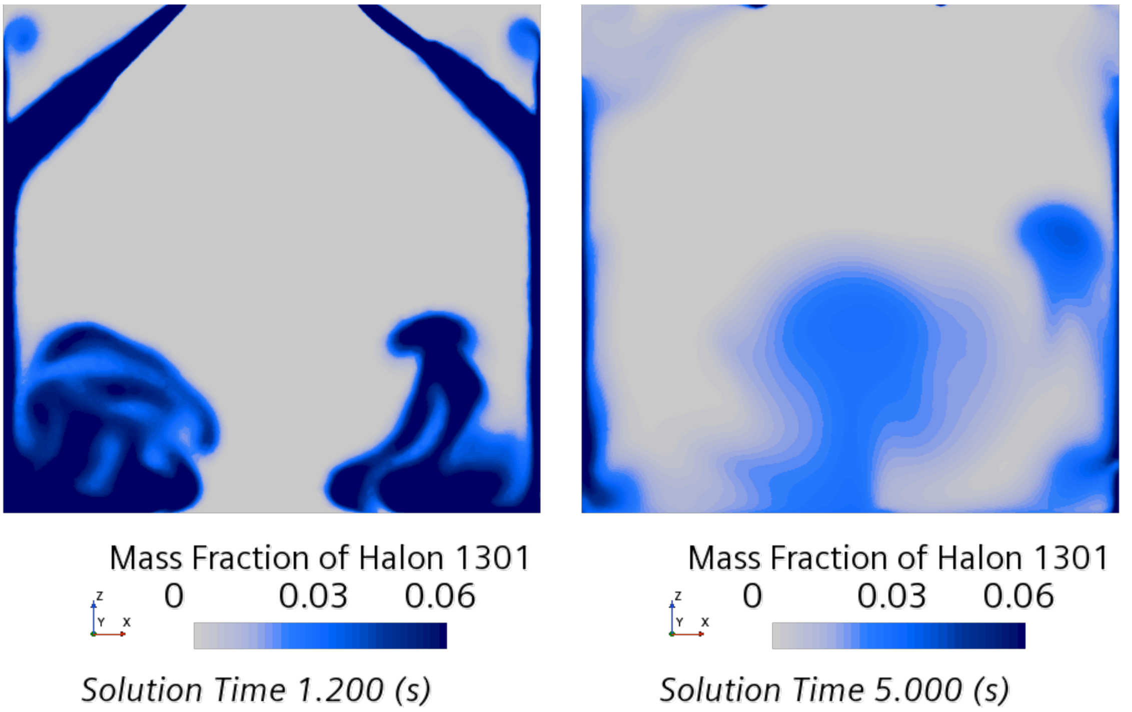

(c) *Mass fraction of Halon at Y=0 after 1.2 seconds.* **(d)** *Mass fraction of Halon at Y=0 after 5 seconds.*

Figure 4.8: *Mass fractions of Halon for angled inlet flow at Y=0 after 0.2-5 seconds, demonstrating the distribution in the cargo compartment.*

In Figure 4.9 and 4.10, the distribution and concentration of the Halon can be seen for a few different planes in the X and Y direction respectively, after 1.2, 3 and 5 seconds. In Figure 4.8b, 4.8c and 4.9b, it can be seen how the Halon mainly spreads downwards after hitting the wall. Only a very small amount of the discharged Halon moves upwards. When traveling downwards along the wall, the Halon begins spinning backwards. The rotation continues after hitting the floor, which seemingly helps distribute the Halon into the middle of the compartment. Comparing the cut-planes in Figure 4.9c and 4.9d with 4.10a and 4.10b respectively, the Halon has clearly distributed into a larger area of the compartment after 5 seconds. However, referring to the colourbar, a small part of the domain reach the required concentration of 5%.

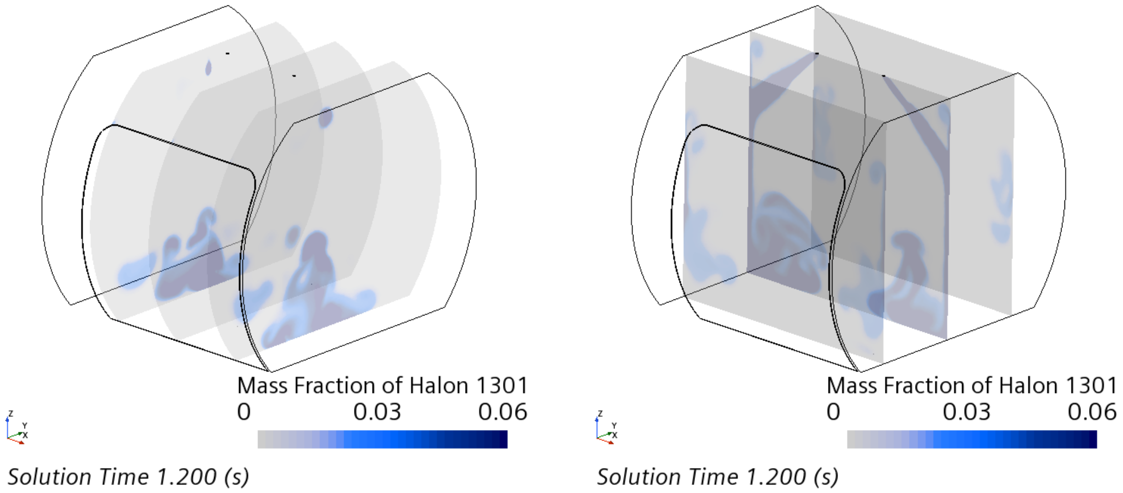

(a) *Mass fraction of Halon at 3 equidistant X-planes after 1.2 seconds.*

(b) *Mass fraction of Halon at 3 equidistant Y-planes after 1.2 seconds.*

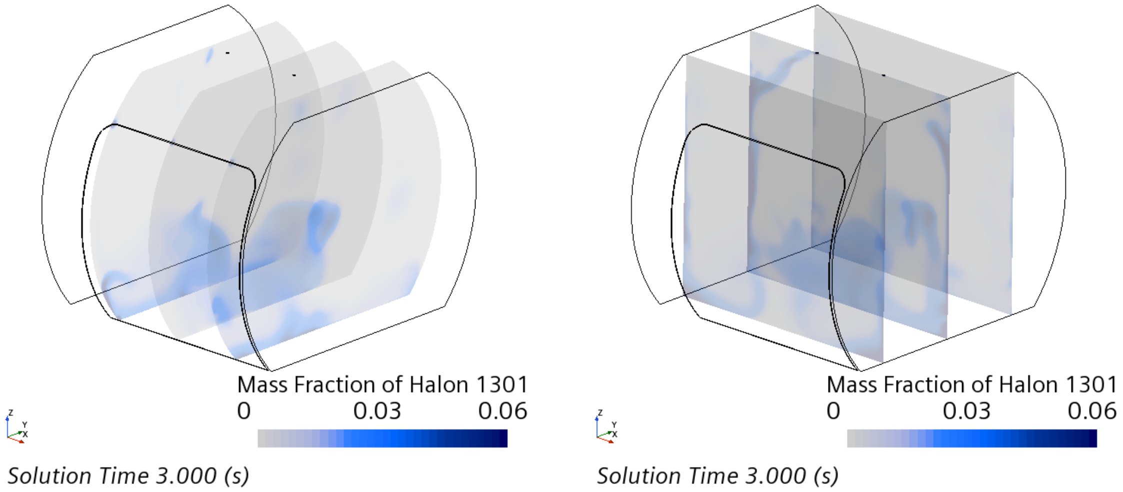

(c) *Mass fraction of Halon at 3 equidistant X-planes after 3 seconds.*

(d) *Mass fraction of Halon at 3 equidistant Y-planes after 3 seconds.*

Figure 4.9: *Mass fractions of Halon for angled inlet flow for equidistant planes normal to X- and Y-direction after 1.2 and 3 seconds, demonstrating the distribution in the cargo compartment.*

The measured concentration is more clearly presented in Figure 4.11, which demonstrates the readings from the probes. Only probe 14 and 15 manage to reach the required value of 5%, peaking at 17.2% and 16.3% respectively. Probe 13 does come close to the limit, reaching 4.5% although much later than probe 14 and 15. Coincidentally, probe 14 and 15 are placed in an area where the inlet flow rotates and disperses. The rest of the probes only reach concentration peaks between 1-4%, with most values below 2%, indicating quite poor dispersion. However, when the angled inlet case is compared to the case with straight inlet flow, there are 5 more probes that register at least 0.1% Halon, totalling 14 probes.

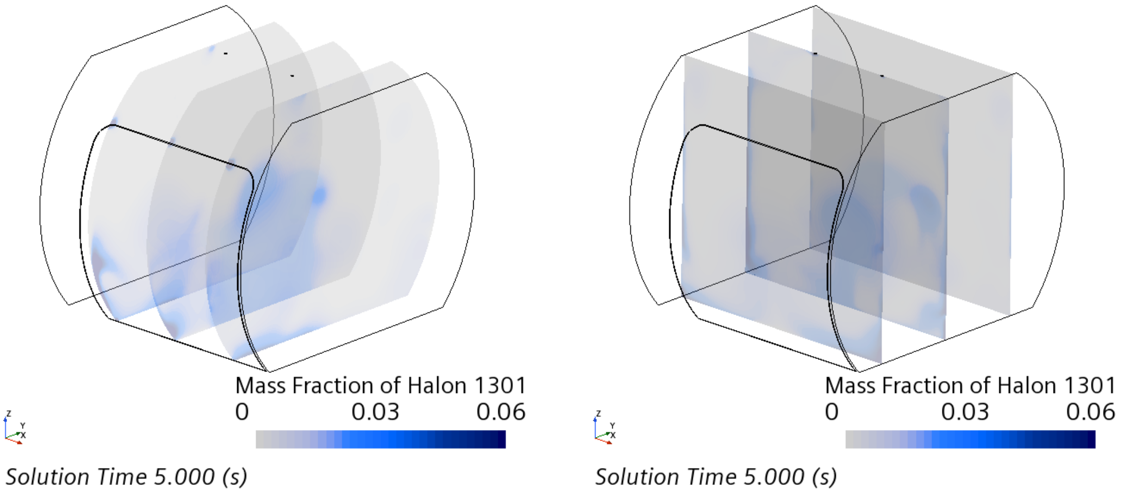

(a) *Mass fraction of Halon at 3 equidistant X-planes after 5 seconds.*

(b) *Mass fraction of Halon at 3 equidistant Y-planes after 5 seconds.*

Figure 4.10: *Mass fractions of Halon for angled inlet flow for equidistant planes normal to X- and Y-direction after 5 seconds, demonstrating the distribution in the cargo compartment.*

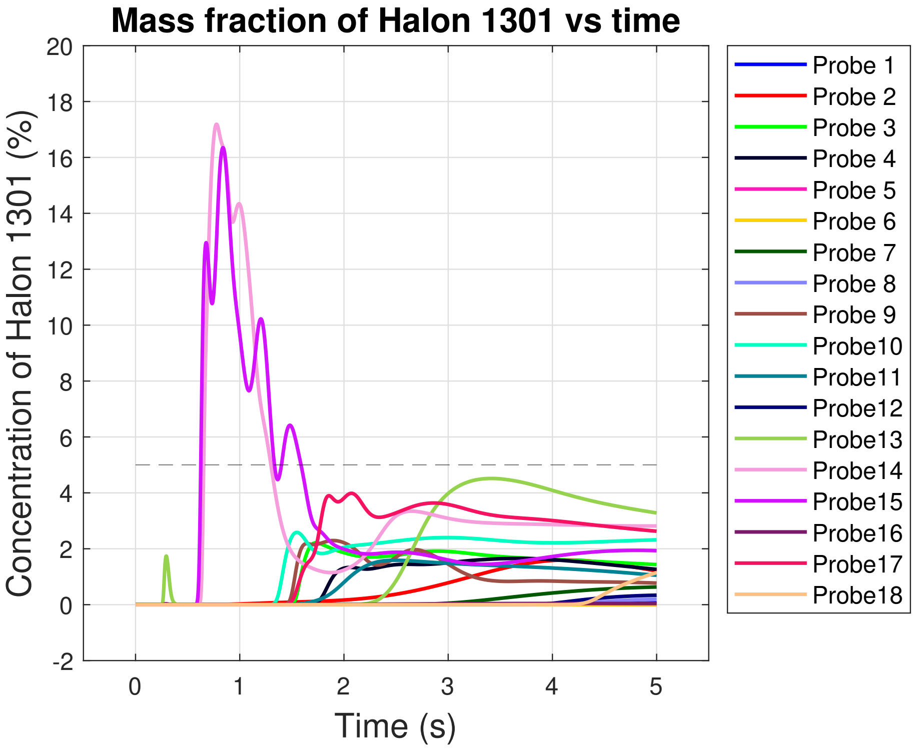

Figure 4.11: *Halon concentration measured by probes for angled inlet flow. Dashed line demonstrating the required 5% concentration level.*

4.2.2.2 Nozzles Angled 45 Degrees

Adding an angled nozzle into the domain produced slightly different results compared to only angling the inlet flow direction, although with some common flow trends. In Figure 4.12, the Halon distribution for some critical events of the simulation is presented visually by the Halon mass fraction. At first sight, the rotating flow pattern appears similar between Figure 4.8 and 4.12, i.e. without and with a nozzle added to the angled inlet flow.

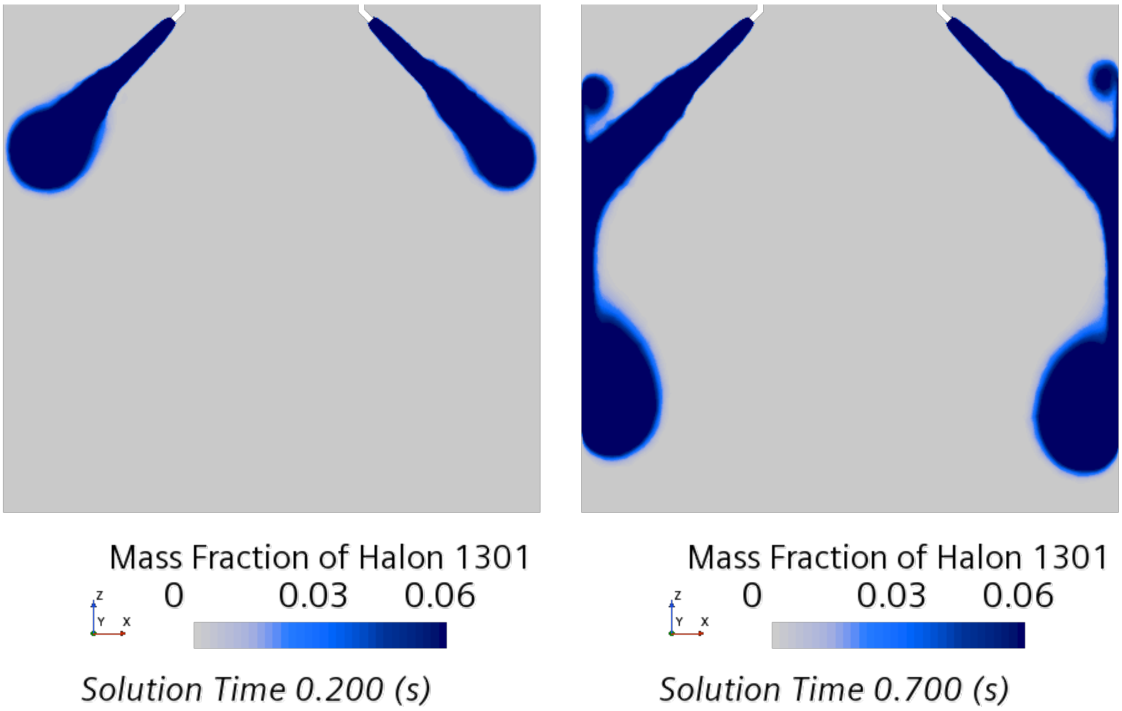

(a) *Mass fraction of Halon at Y=0 after 0.2 seconds.*

(b) *Mass fraction of Halon at Y=0 after 0.7 seconds.*

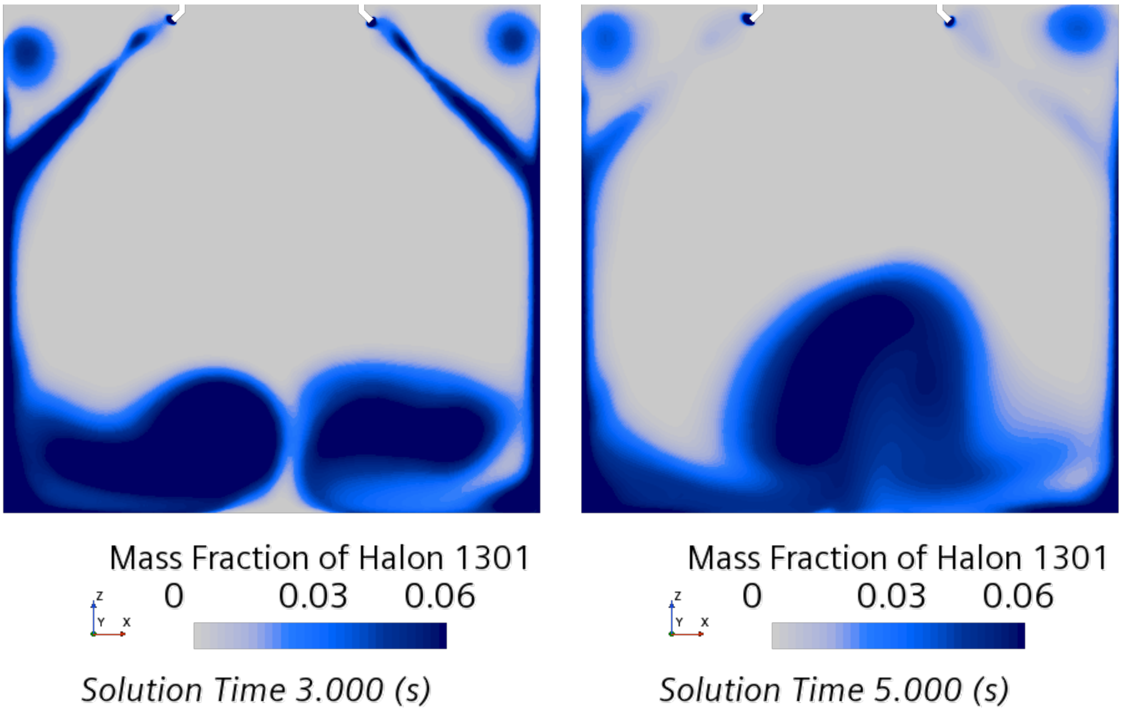

(c) *Mass fraction of Halon at Y=0 after 3 seconds.*

(d) *Mass fraction of Halon at Y=0 after 5 seconds.*

Figure 4.12: *Mass fractions of Halon for 45 degree angled nozzles at Y=0 after 0.2-5 seconds, demonstrating the distribution in the cargo compartment.*

In Figure 4.13 and 4.14, the same X and Y-planes, including different time durations, are presented similar to Figure 4.9 and 4.10. Again, it can be observed from Figure 4.12b, 4.12c and 4.13b, that Halon hits the wall as a concentrated stream, before mostly spreading downwards. Although, there is slightly more Halon that creeps up along the wall and begins rotating back after adding a nozzle. Figure 4.12d, 4.14a and 4.14b, show that Halon has formed a larger, more concentrated, cloud close to floor, compared to the same figures for the angled inlet flow presented in Section 4.2.2.1. Although, comparing the X-planes in 4.13c and 4.9c, the Halon seems to be less dispersed when adding nozzles. The lesser dispersion is even more evident when comparing the X and Y-planes of 4.14a and 4.14b to 4.10a and 4.10b. In the case of angled nozzles, the rotation and dispersion pattern seems to have formed a concentrated sphere of Halon after 5 seconds, with much less Halon in the volume surrounding the sphere.

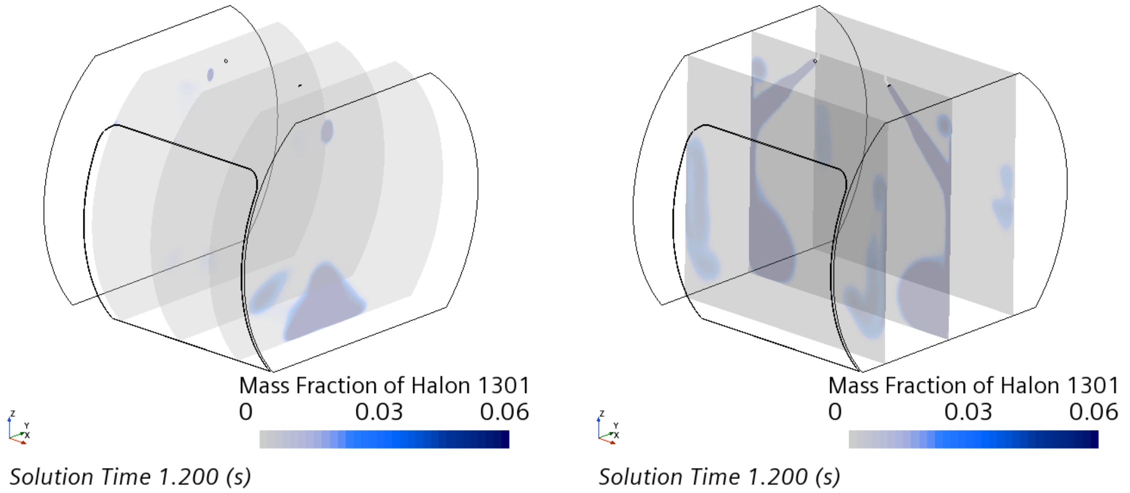

(a) *Mass fraction of Halon at 3 equidistant X-planes after 1.2 seconds.*

(b) *Mass fraction of Halon at 3 equidistant Y-planes after 1.2 seconds.*

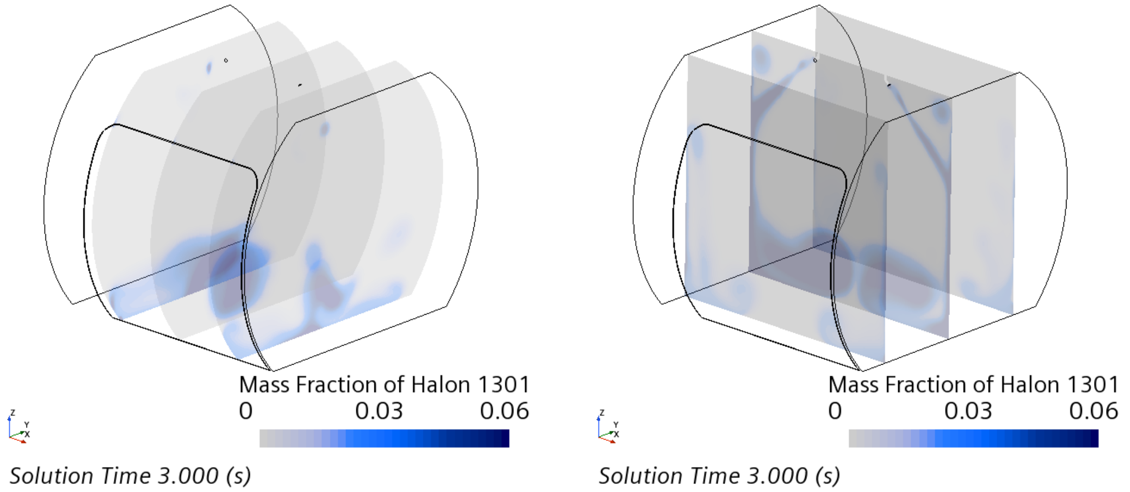

(c) *Mass fraction of Halon at 3 equidistant X-planes after 3 seconds.*

(d) *Mass fraction of Halon at 3 equidistant Y-planes after 3 seconds.*

Figure 4.13: *Mass fractions of Halon for 45 degree angled nozzles for equidistant planes normal to X- and Y-direction after 1.2 and 3 seconds, demonstrating the distribution in the cargo compartment.*

Figure 4.15 shows the exact concentration measured at the probes. Once more, probe 14 and 15 exhibit the largest concentrations since they are placed in an area where the Halon mainly travels, reaching 17.9% and 15.4% concentration respectively. These concentrations are equal in magnitude to the angled inlet flow case. Probe 17 also manages to reach the requirement, peaking at 5.2% concentration. However, 5% concentration is reached much later than for probe 14 and 15. The reason for this is that the flow reaches the position of probe 17, i.e. at the center of the floor, later than probe 14 and 15 located in the front lower corners at the floor. This is clearly seen in Figure 4.12c, where the rotating flow pattern starts in the corner before propagating Halon into the center of the floor. When counting how many

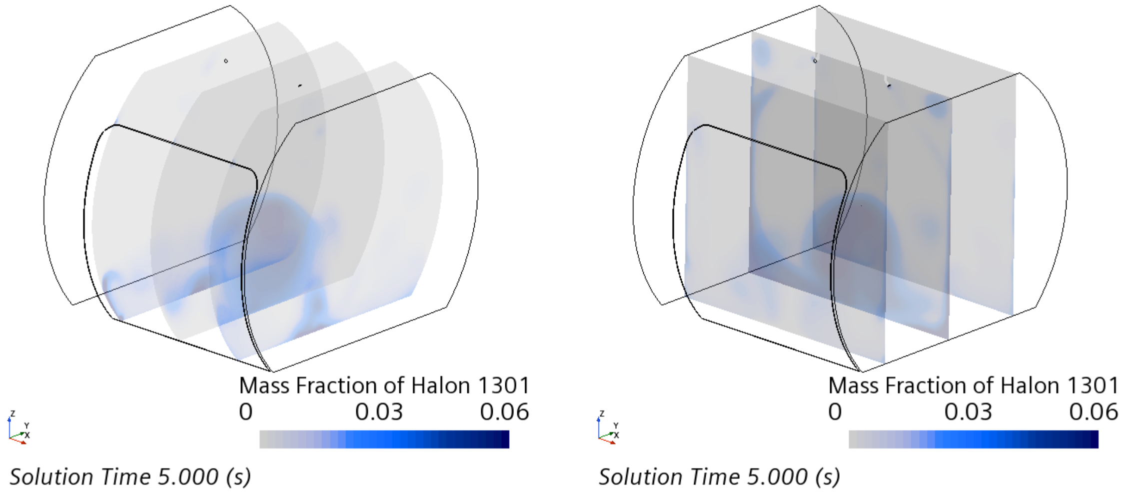

(a) *Mass fraction of Halon at 3 equidistant X-planes after 5 seconds.*

(b) *Mass fraction of Halon at 3 equidistant Y-planes after 5 seconds.*

Figure 4.14: *Mass fractions of Halon for 45 degree angled nozzles for equidistant planes normal to X- and Y-direction after 5 seconds, demonstrating the distribution in the cargo compartment.*

probes measured at least 0.1% Halon, 11 probes managed to register such a value, which is 3 probes less than for the angled inlet case. As is fairly obvious, only 3 probes register above 5% concentration. This is as many probes that registered Halon for the angled inlet flow case.

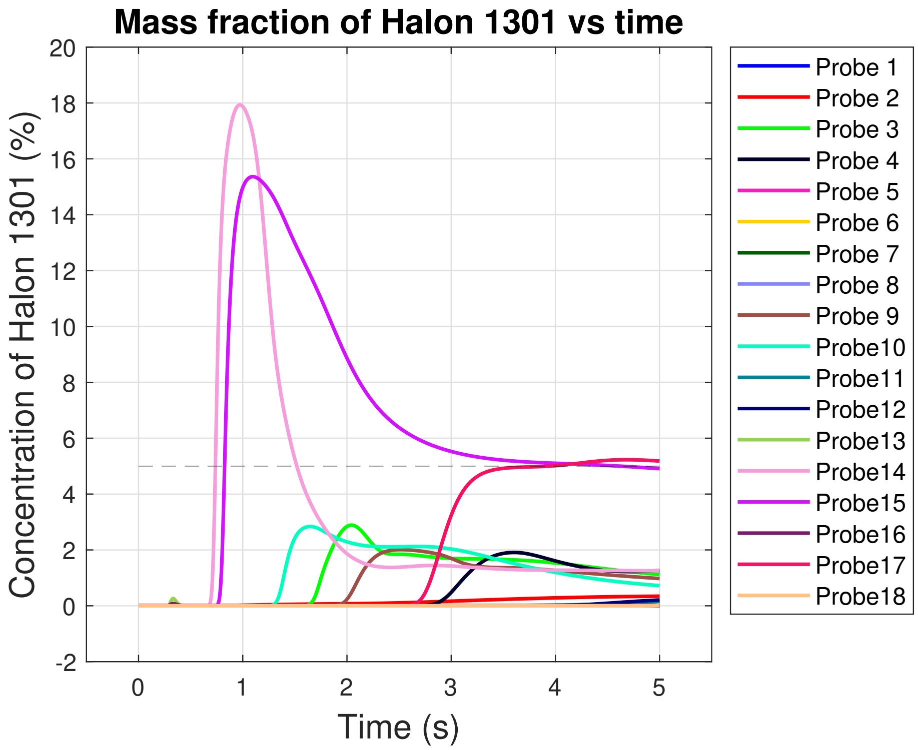

Figure 4.15: *Halon concentration measured by probes for 45 degree angled nozzles. Dashed line demonstrating the required 5% concentration level.*

4.2.2.3 Nozzles Angled 90 Degrees

When the added nozzles are angled by 90 degrees instead of 45, the distribution of Halon is completely different. Naturally, the Halon is quickly expelled along the ceiling, only moving downwards when hitting the wall. This is clearly seen in Figure 4.16.

Additionally, from Figure 4.17 and 4.18, it can be inferred that the Halon spreads not only downwards but also laterally in the Y-direction along the wall, since all three Y-planes show some presence of Halon. Similar to the previous test cases, the Halon begins rotating backwards while spreading along the walls. For all time durations, comparing the X-planes in Figure 4.17 and 4.18 to those in Figure 4.13 and 4.10, there is a notable difference in the distribution of Halon along the side linings. For this case, the Halon manages to spread along the door and side linings, where there is basically no Halon registered in the 45 degree angled cases.

Figure 4.19 demonstrates the measured concentration at the probes. Compared to the concentrations of the previous cases in Figure 4.11 and 4.15, there are no probes which peak at a considerably larger value than others. Probe 2, 7 and 8 have the largest peaks at 7.5%, 8.3% and 8.6% concentration respectively. Out of the 18 probes, 11 measures a value above 0.1%. More importantly, 7 out of those 11 probes registers a peak above 5%. It is the highest number of probes that recorded such high concentrations of Halon, of all simulations - with as well as without angled inlet flow or nozzle.

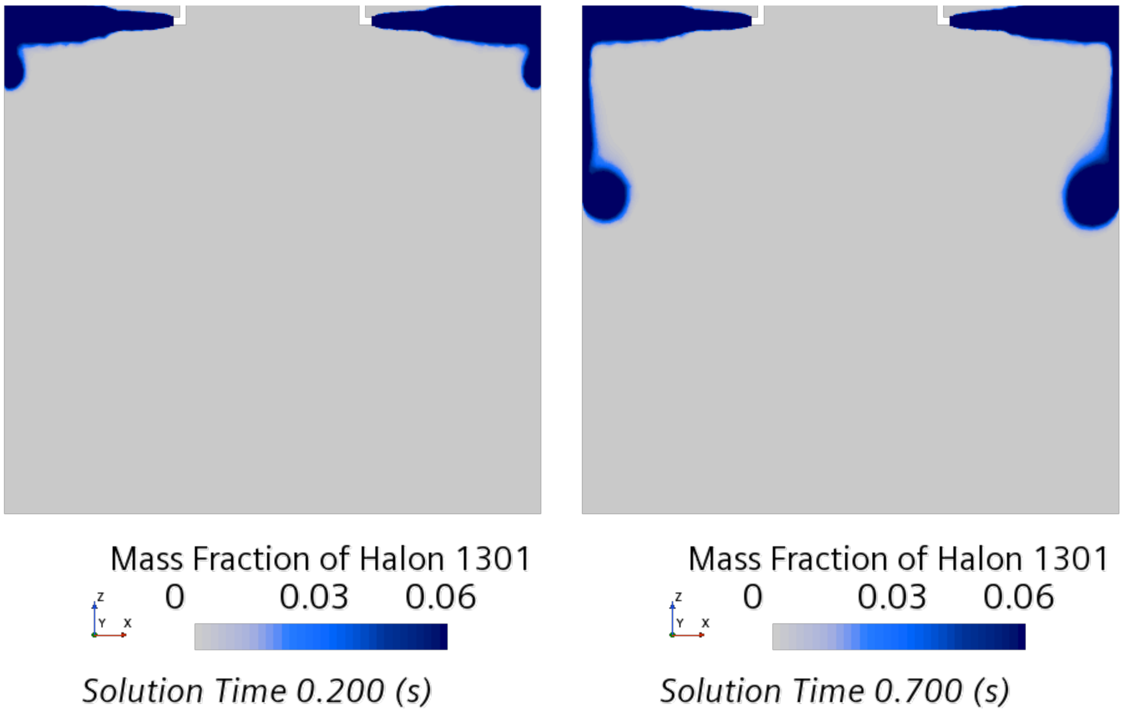

(a) *Mass fraction of Halon at Y=0 after 0.2 seconds.* **(b)** *Mass fraction of Halon at Y=0 after 0.7 seconds.*

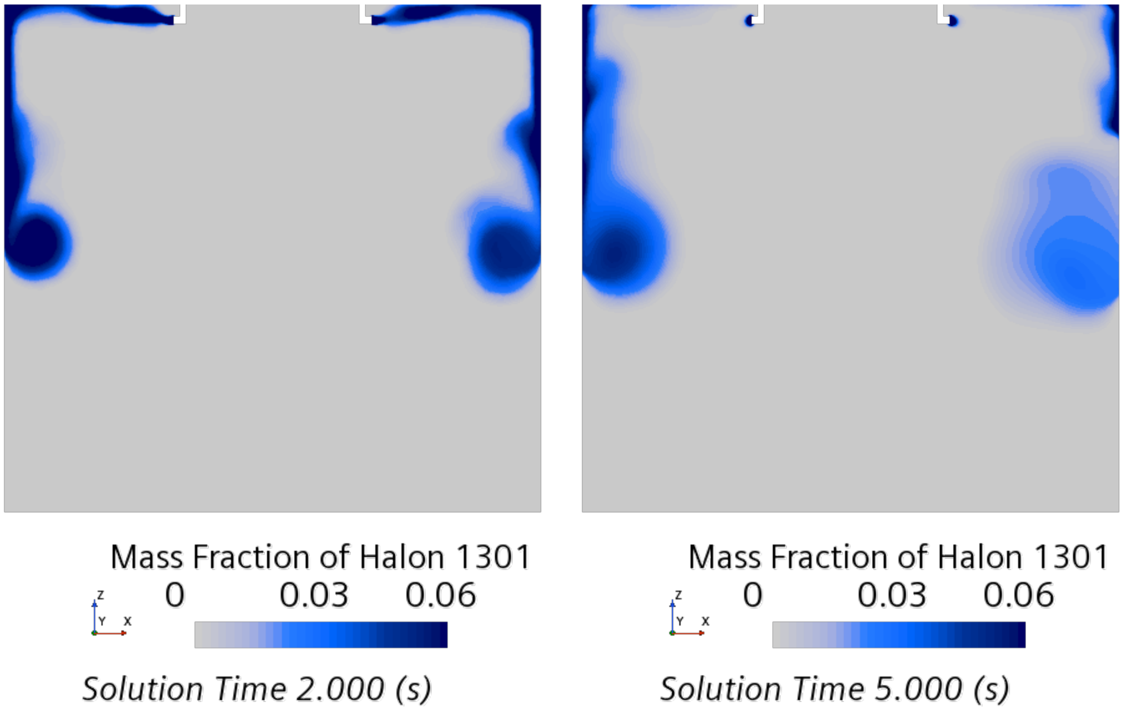

(c) *Mass fraction of Halon at Y=0 after 2 seconds.* **(d)** *Mass fraction of Halon at Y=0 after 5 seconds.*

Figure 4.16: *Mass fractions of Halon for 90 degree angled nozzles at Y=0 after 0.2-5 seconds, demonstrating the distribution in the cargo compartment.*

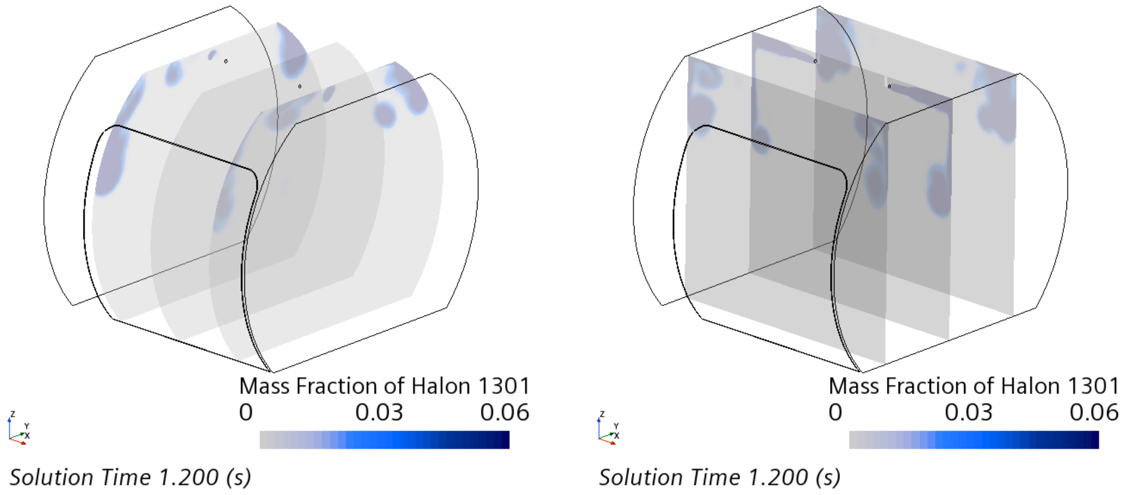

(a) *Mass fraction of Halon at 3 equidistant X-planes after 1.2 seconds.*

(b) *Mass fraction of Halon at 3 equidistant Y-planes after 1.2 seconds.*

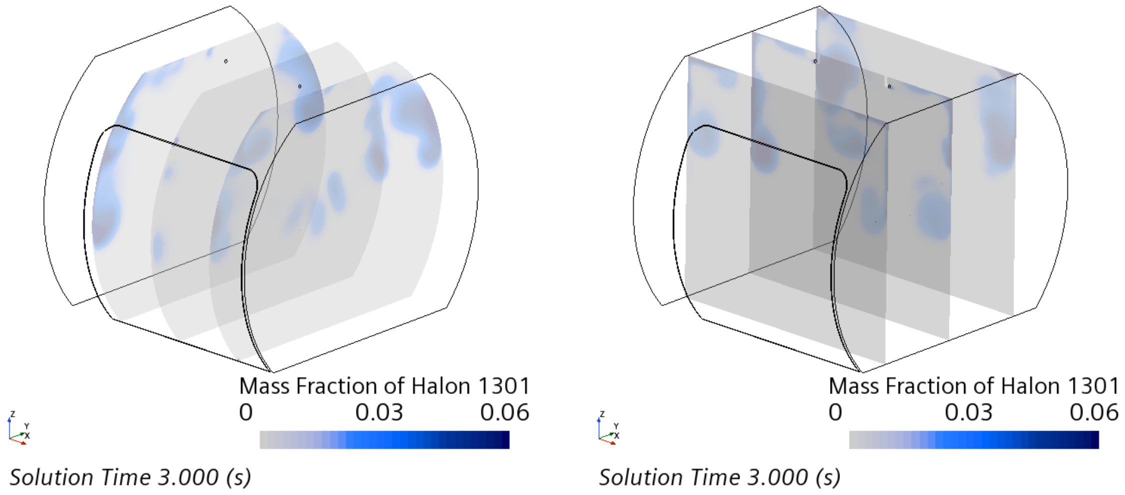

(c) *Mass fraction of Halon at 3 equidistant X-planes after 3 seconds.*

(d) *Mass fraction of Halon at 3 equidistant Y-planes after 3 seconds.*

Figure 4.17: *Mass fractions of Halon for 90 degree angled nozzles for equidistant planes normal to X- and Y-direction after 1.2 and 3 seconds, demonstrating the distribution in the cargo compartment.*

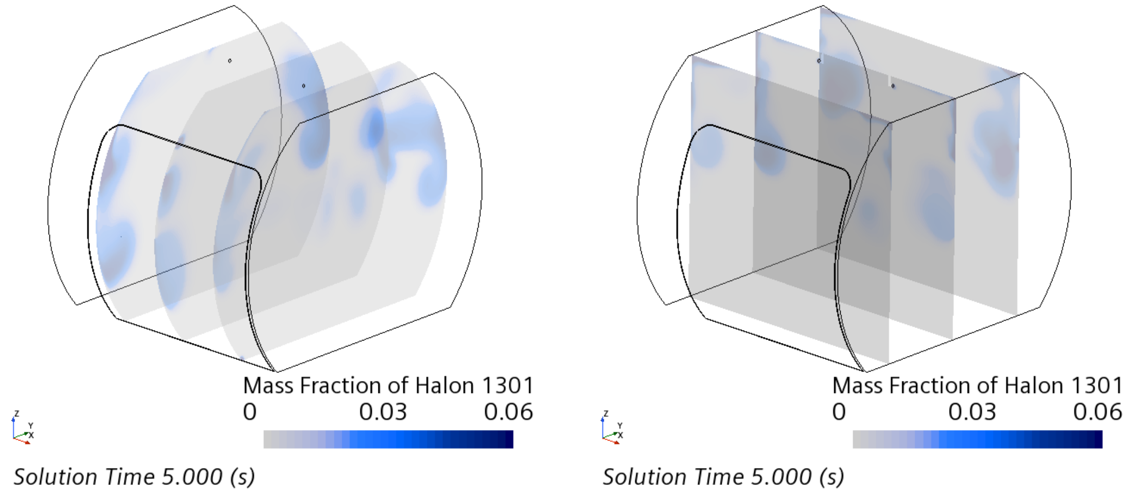

(a) *Mass fraction of Halon at 3 equidistant X-planes after 5 seconds.*

(b) *Mass fraction of Halon at 3 equidistant Y-planes after 5 seconds.*

Figure 4.18: *Mass fractions of Halon for 90 degree angled nozzles for equidistant planes normal to X- and Y-direction after 5 seconds, demonstrating the distribution in the cargo compartment.*

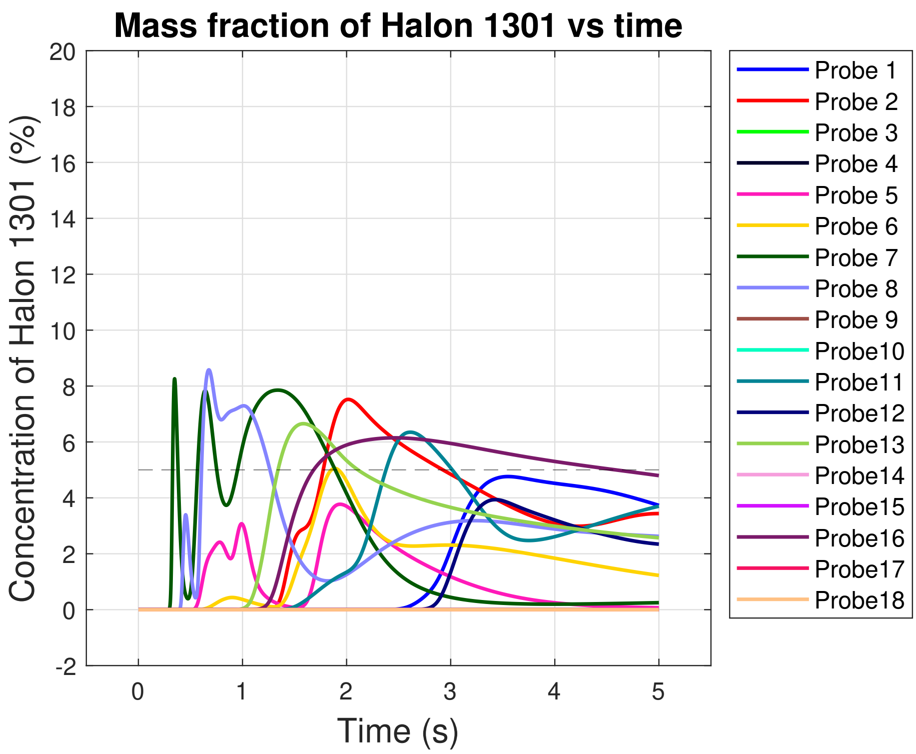

Figure 4.19: *Halon concentration measured by probes for 90 degree angled nozzles. Dashed line demonstrating the required 5% concentration level.*

The mass flow through the door sealing is monitored for all simulation cases. In Figure 4.20, the door sealing mass flow is presented. All simulations give the same results, i.e. a peak mass flow of 2.3 g/s. As mentioned in Section 3.2.2, the total expected mass flow out of the compartment is 9.3 g/s, based on previous experience. The probable reason why the expected mass flow is not achieved is because the model only takes air leakage around the door into account and that the model does not include a source that maintains pressurisation, which results in pressure equalization between the inside and outside of the aircraft. In reality, a leakage is expected around, among other things, wall panels and the pressure valve into the compartment. There is also no pressure equalisation between the inside and outside of the aircraft, as a compressor will maintain pressurisation of the cargo.

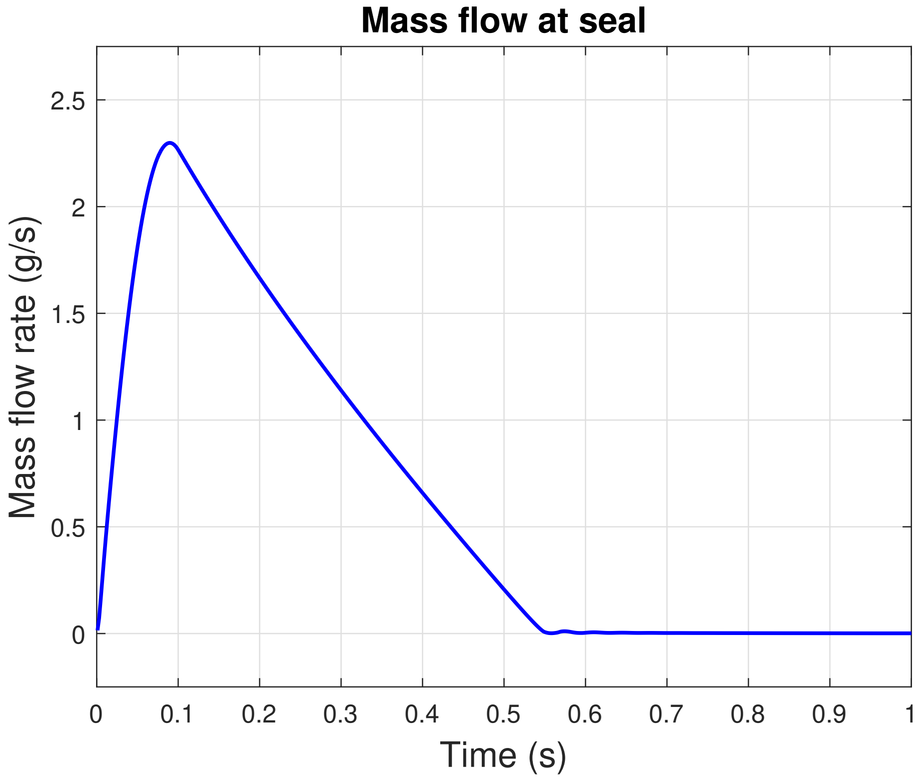

Figure 4.20: *Simulated mass flow rate through door sealing.*

5

Discussion

In this chapter the overall challenges of the thesis are discussed. The challenges mainly focus on methodology approach as well as the overall results, rooted in the novelty of the project.

5.1 Challenges with Bottle and Piping Model

Many issues were encountered in the development of the model which simulates the bottle and piping system. In its current state the model is incomplete, as some issues still need resolving.

One of the difficulties with the model is dealing with the large pressure difference, following the high initial pressure and atmospheric pressure outlet. The instabilities were dampened by both the ramping boundary condition and the adaptive time step, however it is still likely the intense pressure gradient is causing numerical instability. The small geometry of the piping and nozzle combined with high pressure and therefore large velocity probably exacerbates the problem.

Another issue with the model is the time span until the bottle is empty. According to the study by Elliott et al. [24], the majority of the bottle is empty of Halon after 0.24 seconds, which is over double the resulting duration observed from simulation. However, the piping contains Halon for a longer period than the study, as it is empty after close to 0.86 seconds. From experiments in the study, the expected time was 0.58 seconds.

Interestingly, the emptying of the bottle coincides partly with the deviations found in the simulated bottle pressure when compared to experimental data. The deviations between 0.15 and 0.25 seconds occurs simultaneously as the last remaining Halon exits the bottle into the piping. As this happens, nitrogen must move or decompress to replace the volume left by the Halon as it exits. Maybe this exchange affects the simulation. Also, some local backflow could be induced if the simulation somehow calculates higher pressure in some small locations of the piping, which could affect the bottle pressure. Although, it is difficult to conclude any specific reason for the differing results.

A major problem was encountered with diverging turbulence dissipation rate residuals. Filtering for cells with large local residuals showed that several cells of the core volume mesh experienced larger residuals. Interestingly, the cells which showed large local residuals coincided with cells of which there was very little Halon present. A theory is prismatic layers set up for Halon are not immediately compatible for nitrogen.

Finally, issues were increasingly apparent when the domain empties of Halon. It was noted that as the amount of Halon in the system decreased, the amount of iterations required per time step would occasionally increase. This indicates the solver is struggling with some component of the governing equations, which might be related to the amount of Halon left in the system. Eventually, the simulation diverges completely and a floating point error occurs. Observing the few iterations before the floating point error, the system was almost completely empty of Halon. One guess is that the model, possibly the VOF method, cannot solve the governing equations properly when only one phase is present and the other “runs out”. However, when testing both EMP and MMP similar issues still appeared as the bottle emptied.

5.2 Challenges with Cargo Compartment Model

The project resulted in a functioning model of the cargo compartment, being able to run for a handful of inlet flow and nozzle configurations. Two of the main, also connected, issues encountered when developing this model was generating a good quality mesh and thereby ensuring convergence. This was handled in such a way that the simulation was stopped as soon as divergence was detected, given that the simulation had run a couple of hundred iterations. Consequently, bad cells could be detected at the stopped iteration and divergence. It mainly resulted in the mesh having to be locally refined around the nozzles and the door sealing. By refining the mesh there, the model was able to capture the high pressures and velocity gradients in these regions, leading to convergence of the model. In addition to this, the core cells of the compartment were reduced in size to improve convergence and accuracy of the model. To quicken convergence and make the simulation more stable, the cargo compartment simulation was first run during steady-state conditions before changing to unsteady.

Regarding the mesh, it was not realized until after running the simulations that the volumetric controls locally refining the mesh near the inlets and the discharge, described in Section 3.3.2.1, should have been angled as the inflow was being angled. This probably would not have made a huge difference to the overall flow behaviour, but should still have been done to increase the accuracy in that flow region. Fortunately, the volumetric control regions were also large enough to at least partly cover the immediate region where the Halon is discharged.

Additionally, the mesh study performed was limited. It cannot be stated with full confidence that the results are entirely mesh independent. More mesh sizes should have been tested, but presenting some initial results was deemed of greater value. As for why the fourth mesh presented differed in results, a possible reason could stem from the implicit discretisation of the governing equations. The linear system created from the discretisation is sparse, which implies properties of a cell will only affect the closest neighbouring cells. Therefore, the propagation of information and the resulting solution, is slower when the mesh resolution is increased, requiring more iterations. While iterations are different from time steps, it could be possible the slower propagation of information is still in effect.

Another problem with the cargo compartment model is that it is not validated. There was no study nor experimental test found of a cargo compartment firex system to replicate and thereby validate the simulation model for. As mentioned earlier in the report, neither the aircraft nor the cargo compartment exist at the time of the thesis and therefore experimental data of the system is also missing. This meant that validation against experimental data could only be carried out for the bottle and piping system model. When experimental data on the cargo compartment firex system is available, validation work of the model will be required.

An additional challenge has been the computing power and time taken to run the simulations. Despite utilising 128 cores from a high-performance computing cluster, a 5 second simulation of the cargo compartment took 13 hours to run. One reason is due to the amount of iterations needed per time step and the size of each time step. Since a time step of 1E-3 seconds was combined with 5 iterations per time step, 50000 iterations are required to simulate 5 physical seconds. In addition, having to consider two different fluids increases the complexity of the governing equations, likely resulting in a slightly longer solving time per iteration.

Overall, it is important to highlight the novelty of the process in the thesis. As mentioned briefly in Chapter 1 of the report, the lack of established procedures and methodologies in a start-up company as well as applying CFD simulation in a new application area is challenging, especially with the short time frame that this thesis covers. The model and results should be considered as a first model of the system that will need to be improved as well as validated in order to be used as a conceptual design tool. While a few mistakes were made during the development of the model, such mistakes also highlight what does not need to be attempted again. Missteps during this work may create a framework, to be used as guidance for future applications of CFD on firex systems.

6

Conclusion

This chapter summarizes the results obtained in the thesis and presents future work that includes both further development of the current cargo compartment model and the potential to apply CFD simulations in other areas of fire safety systems.

Two three dimensional CFD models were developed for modeling the firex system, where the bottle and piping system is separated from the cargo compartment. The first model considering the bottle and piping, demonstrated some potential for evaluating the flow rate of Halon entering the cargo, but showed too many issues to be considered trustworthy. The pressure drop in the bottle correlated decently, but the simulated flow rate is questionable. The second model representing the cargo compartment, showed potential to be adjusted in terms of flow configurations and should therefore be able to be optimized for future design of the system.

For the cargo simulation results, a nozzle with a 90 degree angle is found to be most effective for fire extinguishing agent distribution. With the 90 degree angled nozzle, 11 of 18 probes recorded Halon after just 5 seconds of simulation. Also noteworthy was that 7 of these 11 probes measured more than the volume concentration requirement of 5%. For the straight inlet flow simulation, only 9 probes registered Halon after 10 seconds. Out of these 9 probes, only 3 probes measured more than 5% concentration. By discharging the Halon straight into the compartment, only the rotating flow pattern at the bottom of the compartment contributes to the Halon distribution. As soon as the inlet flow is angled, Halon is spread more evenly with the help of both spreading along the walls and through rotation at the walls and the floor. Comparing the simulation of the inlet flow case with the nozzle, both angled 45 degrees, 3 more probes registered Halon in the angled inlet flow case. The reason behind it is difficult to conclude, but it can be stated that by adding a nozzle into the compartment, the flow and its characteristics are affected.

While physically reasonable, the simulations do not reflect typical test results. Typically, the peaks in concentration measured by the probes will all occur in a short time frame. However, the simulations showed peaks occuring after very different durations. Even for the case with 90 degree angled nozzles, the peaks should be expected to appear either simultaneously or with great overlap. The main reason is likely due to the bottle parameters used to prescribed the inlet flow being taken from an APU application and not from a cargo application. For the cargo, a lower bottle pressure and larger filling mass is typical. Such conditions may improve Halon distribution. A lower pressure might not drive the Halon immediately downwards as seen in the simulation results obtained, but instead spread it more evenly in the compartment as the heavier density of Halon forces it to sink towards the ground. An increased filling mass should simply mean there is more Halon available to fill the domain.

Finally, the results also showed that simulating an initial leakage through the door seal is not representative of real ventilation conditions. Since the leakage is only due to the pressure differential caused by initial conditions, the leakage stops as soon as the pressure equalises. In reality, the pressure difference in the cargo is maintained i.e. the leakage should not fade.

6.1 Future Work

For further research within this topic, there are several aspects that would be of interest to add to the cargo compartment simulation model created in this thesis. In addition to the improvements that can be applied to the current simulation model, there are also other application areas within fire protection systems that would be valuable to apply CFD simulation models to. This section is thus divided into two sub sections to distinguish future work on the model developed so far and future work in other areas that are likewise at high risk of catching fire.

6.1.1 Cargo Compartment Model

Since the CFD model developed in this thesis is a first model of the system, some limitations are added to the model. Section 3.3.2.3 describes the initial conditions of the model, including the pressure difference between the cargo compartment and the outside of the aircraft. Since no compressor is included in the model, continuous pressurized air will not be pumped into the cargo compartment. This leads to that the pressure difference between the inside and outside of the aircraft will, after a sufficiently long simulation time, reach pressure equalization in the simulation. To prevent this from happening in future use of the simulation model, another inlet should therefore be applied to the model to maintain the pressurization.

To simulate the air leakage that occurs through the sealing around the door of the cargo compartment, a simple door sealing was added to the CAD model. This sealing, as mentioned in Section 3.2.2, has a width of 5 mm. This is a conservative measure that can be adjusted in future simulations as well, to study the air leakage rate of the compartment. Additional sources of leakage, such as through panels or the pressure valve is also of value to add to the model.

Due to that it is a first model of the system, certain simplifications were necessary. The model is intended to be used in the future for optimization of the firex system. A necessary step before optimizing the firex system is to implement more realistic nozzles to the model. Among other things, several holes are placed circularly around the end of the nozzle in order to spread the Halon in all directions. By adding the complexity of nozzle designs together with different numbers and locations, more realistically applicable designs of the system can be simulated.

The physics models chosen for the cargo compartment simulation consider Halon as a gaseous phase. However, based on experience from fire protection systems engineers, a small amount of Halon remains in liquid state. This results in a vapour phase, which is not considered by the model. Therefore, implementing a method that is able to consider liquid droplets and potential phase changes of such droplets could potentially increase the prediction accuracy. A method that could be implemented is lagrangian particle tracking. With this method, it is possible to track the motion of single particles and their properties. The method also allows for coupling between phases, potentially letting the droplets affect mass and momentum of the continuous gas phase.

For future use of the model, it would be valuable to change the discharge bottle parameters, such as changing the bottle size, the amount of Halon and pressure. This would result in different inlet conditions. Due to limited time, this was not done in the thesis, but it is not difficult to change given the developed model.

As shortly mentioned in Section 2.1.1, the search for a new firex agent is ongoing. When an alternative agent is found, the ambition is that only the material properties of the agent should be changed in the model, given that the phase characteristics are the same and the agent enters the compartment as a gas.

6.1.2 Other CFD Compatible Application Areas

Besides the cargo compartment, there are other application areas to create CFD models and do CFD simulations on within aircraft fire protection systems. This section describes some of these application areas for future work.

6.1.2.1 Auxiliary Power Unit

As mentioned in Section 2.1, the APU is one of the areas of the aircraft more prone to catch fire. For the ES-30, the APU will consist of two turbo generators that, if necessary, will feed the batteries with electricity to propel the aircraft. By definition, the APU compartment is a fire zone, separated from the rest of the aircraft by a firewall. The majority of APU installations are found in the aft of the aircraft, in the so called tailcone, which provides isolation [28]. Due to the presence of fuel and other fluids close to surfaces with very high temperatures, there is a requirement to provide a built-in fire extinguishing system for such a compartment. The APU firex system is usually located in the aft fuselage, close to the APU. If a fire is detected in the APU compartment, the APU will automatically be shut down. The APU firex system works similar to that of the cargo compartment, but unlike the measuring of the firex agent concentration of the cargo compartment, the APU firex agent concentration needs to be minimum 6% by volume. The expected ventilation through the compartment is also higher than for a cargo environment. Due to the APU's risk of catching fire, the similar methods used to extinguish such a fire and the similar tests conducted to verify the system, compared to the cargo compartment, the application of CFD simulation has great potential.

6.1.2.2 Propulsion Batteries

In addition to the cargo compartment and the APU, there is also a new fire risk on the ES-30 compared to conventional aircraft - the batteries. The major safety hazard that arise with li-ion batteries of such size and power is thermal runaway, i.e. an uncontrollable chemical reaction which can cause the battery to catch fire. For large propulsion batteries, such as those used in the ES-30, fire protection regulations are currently being developed with the intent of containing the fire and its propagation, thereby self extinguishing. The only regulations regarding batteries currently presented by authorities are applied to small, portable batteries such as those found in laptops. These regulations are also only directly applicable on vertical take-off and landing aircraft, through an EASA means of compliance. Even though these directives can not be directly applied on the ES-30, they can be used as guidelines of the industry within the area [29] and in which direction the regulations are developing. It is difficult to find a firex agent effective enough to extinguish battery fires of this magnitude, but CFD simulations of alternative agents could be an applicable tool in finding a suitable agent.

6.1.2.3 Smoke Detectors

As mentioned in Section 2.1.2, a Class C compartment, like the cargo compartment on the ES-30, must be equipped with both a fire extinguishing system and a smoke and/or fire detection system. A future application area may therefore be to simulate smoke development and dispersion inside the cargo compartment using CFD as a tool.

Bibliography

[1] Brandon Graver, Ph.D., Kevin Zhang, Dan Rutherford, Ph.D, “Co2 emissions from commercial aviation, 2018,” Sep. 2019. [Online]. Available: `https://theicct.org/wp-content/uploads/2021/06/ICCT_CO2-commercl-aviation-2018_20190918.pdf` (visited on 02/13/2023).

[2] I. Tiseo, “Breakdown of co2 emissions in the transportation sector worldwide 2020, by subsector,” Feb. 2023. [Online]. Available: `https://www.statista.com/statistics/1185535/transport-carbon-dioxide-emissions-breakdown/` (visited on 02/13/2023).

[3] Federal Aviation Administration, “Faa aerospace forecast - fiscal years 2022-2042,” 2022. [Online]. Available: `https://www.faa.gov/sites/faa.gov/files/2022-06/FY2022_42_FAA_Aerospace_Forecast.pdf` (visited on 02/13/2023).

[4] The Swedish Government, “Sweden’s climate policy framework,” 2021. [Online]. Available: `https://www.government.se/articles/2021/03/swedens-climate-policy-framework/` (visited on 02/13/2023).

[5] The Guardian, “Norway aims for all short-haul flight to be 100% electric by 2040,” 2018. [Online]. Available: `https://www.theguardian.com/world/2018/jan/18/norway-aims-for-all-short-haul-flights-to-be-100-electric-by-2040` (visited on 02/13/2023).

[6] European Commission Directorate - General for Mobility and Transport, “Airworthiness - mobility and transport - european union,” [Online]. Available: `https://transport.ec.europa.eu/transport-modes/air/aviation-safety-policy-europe/aviation-safety-rules/airworthiness_en` (visited on 05/04/2023).

[7] Safety first - The Airbus Safety magazine, “Protecting aircraft and passengers from cargo fires,” 2018. [Online]. Available: `https://safetyfirst.airbus.com/protecting-aircraft-and-passengers-from-cargo-fires/` (visited on 02/14/2023).

[8] Heart Aerospace, “Learn more about the es-30,” 2022. [Online]. Available: `https://heartaerospace.com/es-30/` (visited on 02/15/2023).

[9] EASA CS-25 Amendment 27, “Certification specifications and acceptable means of compliance for large aeroplanes (cs-25 amendment 27),” 2023. [Online]. Available: `https://www.easa.europa.eu/en/document-library/certification-specifications/cs-25-amendment-27` (visited on 02/20/2023).

[10] SKYbrary, “Halon fire extinguishers,” [Online]. Available: `https://www.skybrary.aero/articles/halon-fire-extinguishers` (visited on 02/16/2023).

[11] ICAO, "Aircraft halon replacement. assembly - 41st session. working paper. technical commission," 2022. [Online]. Available: `https://www.icao.int/Meetings/a41/Documents/WP/wp_096_en.pdf`.

[12] Boeing, "Fire protection: Cargo compartments," 2010. [Online]. Available: `https://www.boeing.com/commercial/aeromagazine/articles/2011_q2/3/#fig1` (visited on 02/20/2023).

[13] Federal Aviation Administration, "Advisory circular ac 25.851-1 - built-in fire extinguishing/suppression systems in class c and class f cargo compartments," [Online]. Available: `https://www.faa.gov/documentLibrary/media/Advisory_Circular/AC_25.851-1.pdf`.

[14] SKYbrary, "Aircraft hold fire risks," [Online]. Available: `https://www.skybrary.aero/articles/aircraft-hold-fire-risks` (visited on 02/22/2023).

[15] Volupe Engineering Software, "Multiphase modeling capabilities in simcenter star-ccm+," [Online]. Available: `https://volupe.se/multiphase-modeling-capabilities-in-simcenter-star-ccm/` (visited on 05/16/2023).

[16] F. Menter, *American Institute of Aeronautics and Astronautics Journal*, vol. 32, no. 8, pp. 1598–1605, Aug. 1994.

[17] CFD Online. "K-epsilon models." (2011), [Online]. Available: `https://www.cfd-online.com/Wiki/K-epsilon_models` (visited on 03/31/2023).

[18] CFD Online. "K-omega models." (2011), [Online]. Available: `https://www.cfd-online.com/Wiki/K-omega_models` (visited on 03/31/2023).

[19] W. L. Oberkampf and T. G. Trucano, "Verification and validation in computational fluid dynamics," *Progress in Aerospace Sciences*, vol. 38, no. 3, pp. 209–272, 2002, ISSN: 0376-0421. DOI: `https://doi.org/10.1016/S0376-0421(02)00005-2`. [Online]. Available: `https://www.sciencedirect.com/science/article/pii/S0376042102000052`.

[20] P. J. Roach, *American Institue of Aeronautics and Astronautics Journal*, vol. 36, no. 5, pp. 696–702, May 1998.

[21] R. Liu, H. Shi, Q. Zhou, W. Ma, T. Wang, and S. Lu, "Simulation of fire extinguishing agent transport and dispersion in aircraft engine nacelle," *Fire*, vol. 5, no. 4, p. 97, Jul. 2022, ISSN: 2571-6255. DOI: `10.3390/fire5040097`. [Online]. Available: `http://dx.doi.org/10.3390/fire5040097`.

[22] J. Kim, B. Baek, and J. Lee, "Numerical analysis of flow characteristics of fire extinguishing agents in aircraft fire extinguishing systems," *Journal of Mechanical Science and Technology*, vol. 23, pp. 1877–1884, 2009. DOI: `https://doi.org/10.1007/s12206-009-0618-7`.

[23] A. Amatriain, G. Rubio, I. Parra, E. Valero, D. Andreu, and P. M. Martín, "Mathematical modeling of nitrogen-pressurized halon flow in fire extinguishing systems," *Fire Safety Journal*, vol. 122, p. 103 356, 2021, ISSN: 0379-7112. DOI: `https://doi.org/10.1016/j.firesaf.2021.103356`. [Online]. Available: `https://www.sciencedirect.com/science/article/pii/S0379711221000977`.

[24] D. Elliott, P. Garrison, G. Klein, K. Moran, and M. Zydowicz, "Flow of nitrogen-pressurized halon 1301 in fire extinguishing systems," Jet Propulsion Laboratory, California Institute of Technology, Tech. Rep., 1984.

[25] C. B. Laney, *Computational Gasdynamics*. Cambridge University Press, 1998. DOI: `10.1017/CBO9780511605604`.

[26] Guilherme Caminha, “The cfl condition and how to choose your timestep size,” [Online]. Available: `https://www.simscale.com/blog/cfl-condition/` (visited on 10/17/2019).

[27] S. CD-adapco, *STAR-CCM+ v.11.02 User Guide*. 2016.

[28] Boeing, “Fire protection: Engines and auxiliary power units,” 2010. [Online]. Available: `https://www.boeing.com/commercial/aeromagazine/articles/2010_q4/3/` (visited on 02/17/2023).

[29] EASA Means of Compliance, “Second publication of means of compliance with the special condition vtol,” 2022. [Online]. Available: `https://www.easa.europa.eu/en/document-library/product-certification-consultations/special-condition-vtol` (visited on 02/20/2023).

DEPARTMENT OF SOME SUBJECT OR TECHNOLOGY
CHALMERS UNIVERSITY OF TECHNOLOGY
Gothenburg, Sweden
www.chalmers.se

CHALMERS
UNIVERSITY OF TECHNOLOGY